RESEARCH ARTICLE

SWI/SNF Complex Mutations Promote Thyroid Tumor Progression and Insensitivity to Redifferentiation Therapies

Mahesh Saqcena[1], Luis Javier Leandro-Garcia[1], Jesper L.V. Maag[2], Vatche Tchekmedyian[3], Gnana P. Krishnamoorthy[1], Prasanna P. Tamarapu[1], Vera Tiedje[1], Vincent Reuter[2], Jeffrey A. Knauf[1], Elisa de Stanchina[4], Bin Xu[5], Xiao-Hui Liao[6], Samuel Refetoff[7], Ronald Ghossein[5], Ping Chi[1], Alan L. Ho[3], Richard P. Koche[2], and James A. Fagin[1,3]

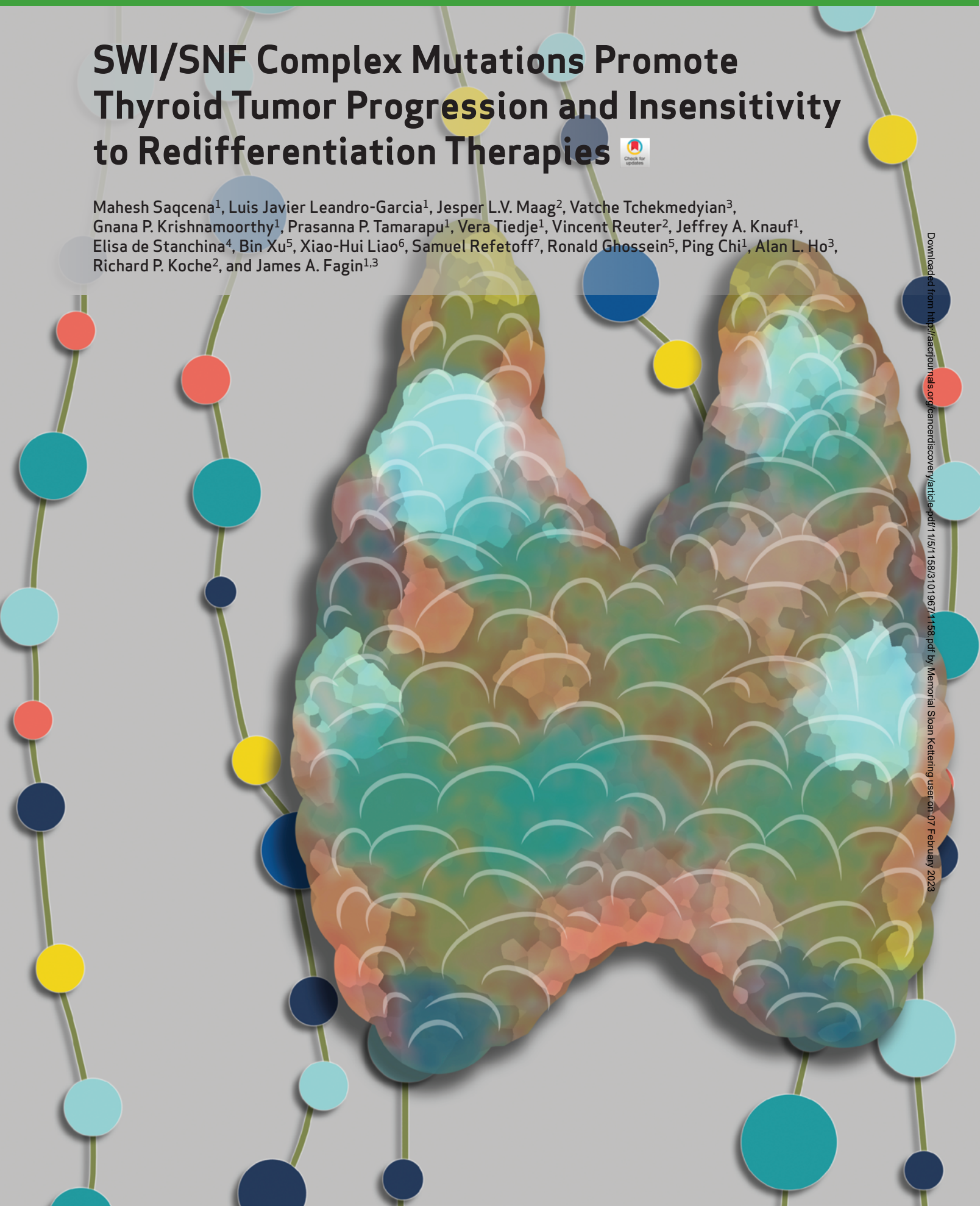

ABSTRACT Mutations of subunits of the SWI/SNF chromatin remodeling complexes occur commonly in cancers of different lineages, including advanced thyroid cancers. Here we show that thyroid-specific loss of *Arid1a, Arid2*, or *Smarcb1* in mouse $BRAF^{V600E}$-mutant tumors promotes disease progression and decreased survival, associated with lesion-specific effects on chromatin accessibility and differentiation. As compared with normal thyrocytes, $BRAF^{V600E}$-mutant mouse papillary thyroid cancers have decreased lineage transcription factor expression and accessibility to their target DNA binding sites, leading to impairment of thyroid-differentiated gene expression and radioiodine incorporation, which is rescued by MAPK inhibition. Loss of individual SWI/SNF subunits in BRAF tumors leads to a repressive chromatin state that cannot be reversed by MAPK pathway blockade, rendering them insensitive to its redifferentiation effects. Our results show that SWI/SNF complexes are central to the maintenance of differentiated function in thyroid cancers, and their loss confers radioiodine refractoriness and resistance to MAPK inhibitor–based redifferentiation therapies.

SIGNIFICANCE: Reprogramming cancer differentiation confers therapeutic benefit in various disease contexts. Oncogenic BRAF silences genes required for radioiodine responsiveness in thyroid cancer. Mutations in SWI/SNF genes result in loss of chromatin accessibility at thyroid lineage specification genes in *BRAF*-mutant thyroid tumors, rendering them insensitive to the redifferentiation effects of MAPK blockade.

INTRODUCTION

Therapeutic interventions to reprogram the differentiation state of cancers have met with considerable success, particularly in the setting of a subset of myeloid malignancies. The prototypic paradigm is acute promyelocytic leukemia (APL) driven by the *PML–RARα* fusion, which is the product of a recombination between the promyelocytic leukemia (*PML*) and the retinoic acid receptor-α (*RARα*) genes. This fusion protein blocks myeloid differentiation at the promyelocytic stage of myelopoiesis (1). Its relief by treatment with all-trans retinoic acid and arsenic trioxide has revolutionized the treatment of the disease (2). Acute myeloid leukemias driven by mutations of the isocitrate dehydrogenase genes *IDH1* and *IDH2* lead to production of the oncometabolite 2-hydroxyglutarate, which alters DNA methylation and impairs differentiation (3, 4). Small-molecule IDH1 and 2 inhibitors induce myeloid differentiation and provide therapeutic benefit for these patients (5).

The differentiation state of thyroid cancers is a critical determinant of their response to medical therapy, because the efficacy of radioiodine (RAI) is dependent on the expression of genes required for iodine uptake, oxidation, and incorporation into tyrosine residues of thyroglobulin. Papillary thyroid cancers (PTC) are the most common form of the disease. They are genetically simple tumors harboring mutations of genes encoding effectors that signal primarily through MAPK (6–8): $BRAF^{V600E}$ (60%), *RAS* (15%), and gene fusions of *BRAF, RET, NTRK*, and *ALK* (12%; ref. 9). Next-generation sequencing studies of poorly differentiated thyroid cancer (PDTC) and anaplastic thyroid cancer (ATC) reveal a more complex picture, characterized by a stepwise increase in mutation burden (10, 11) and progressive accumulation of mutations of the *TERT* promoter and *TP53* (10, 12–15). A particularly salient feature is the development of mutations of genes encoding epigenetic modifiers, most prominently of individual subunits of the SWI/SNF (BAF and PBAF) chromatin remodeling complexes (10). The functional relevance of this finding is supported by an *in vivo* Sleeping Beauty transposon mutagenesis screen that found that disruptions of chromatin modifiers, including SWI/SNF subunits, significantly cooperate with oncogenic HRAS in progression to PDTC (16).

The SWI/SNF complexes consist of 12 to 15 subunits, which when assembled hydrolyze ATP to mobilize nucleosomes and remodel chromatin. SWI/SNF complexes are preferentially targeted to enhancers distal to the transcription start sites of genes, many of which are linked to developmental processes and lineage specification (17). The mSWI/SNF complexes have been classified broadly as BAF (BRG1/BRM-associated factors), PBAF (polybromo-associated factors), and ncBAF (noncanonical BAF) complexes (18, 19). The three complexes share core subunits such as SMARCC1/2 and SMARCD1/2/3, but also contain subunits that are unique to each class: for example, ARID1A or ARID1B in BAF, ARID2

[1]Human Oncology and Pathogenesis Program, Memorial Sloan Kettering Cancer Center, New York, New York. [2]Center for Epigenetics Research, Memorial Sloan Kettering Cancer Center, New York, New York. [3]Department of Medicine, Memorial Sloan Kettering Cancer Center, New York, New York. [4]Antitumor Assessment Core Facility, Memorial Sloan Kettering Cancer Center, New York, New York. [5]Department of Pathology, Memorial Sloan Kettering Cancer Center, New York, New York. [6]Department of Medicine, The University of Chicago, Chicago, Illinois. [7]Departments of Medicine and Pediatrics and the Committee on Genetics, The University of Chicago, Chicago, Illinois.

M. Saqcena and L.J. Leandro-Garcia contributed equally to this work.

Corresponding Author: James A. Fagin, Human Oncology and Pathogenesis Program, Memorial Sloan Kettering Cancer Center, 1275 York Avenue, New York, NY 10065. Phone: 646-888-2136; E-mail: faginj@mskcc.org

Cancer Discov 2021;11:1158–75

doi: 10.1158/2159-8290.CD-20-0735

and PBRM1 in PBAF, and GLTSCR1 and BRD9 in ncBAF (18). Recurrent mutations in genes encoding various subunits of the SWI/SNF complex have been found in ~20% of human cancers across multiple tumor lineages (20, 21). SWI/SNF is antagonistic with the activity of the polycomb repressive complex 2 (PRC2) in development (22) and in certain tumor types (23). Loss of SWI/SNF function has been suggested to promote oncogenesis via derepression of PRC2 and upregulation of a stem cell–associated program (23). Mutations in SWI/SNF create a dependency on EZH2, the catalytic histone methyltransferase subunit of the PRC2 complex (24, 25). The mechanisms by which SWI/SNF mutations cooperate with other oncogenic drivers in disease progression are poorly understood, with growing evidence that this is lineage- and context-dependent (26).

The lineage transcription factors (TF) PAX8, NKX2-1, and FOXE1 are required for thyroid development (27) and for expression of genes involved in thyroid hormone biosynthesis (28). Oncoproteins that activate MAPK signaling impair expression of these genes and their transcriptional targets in thyroid cancers, which renders them unresponsive to RAI therapy. RAF or MEK inhibitors reverse this effect in genetically engineered mouse models of BRAF-induced thyroid cancer (29, 30) and in patients with metastatic disease (31, 32). However, they are ineffective for most patients with PDTC and all patients with ATC.

Here we asked how disruptions of SWI/SNF affect the biology of thyroid cancers and specifically their differentiation state. We demonstrate that disruption of distinct SWI/SNF subunits results in unique chromatin and transcriptional landscapes leading to thyroid dedifferentiation and tumor progression. Importantly, we show that SWI/SNF loss promotes resistance to RAF/MEK inhibitor–based redifferentiation therapies in mice and in selected patients enrolled in clinical trials.

RESULTS

SWI/SNF Subunit Mutations Are Associated with Advanced Forms of Human Thyroid Cancer

PTCs are driven primarily by constitutive MAPK activation, most commonly through $BRAF^{V600E}$ (9). PDTC and ATC have a higher mutation burden (10, 11), including of genes encoding subunits of the SWI/SNF chromatin remodeling complexes (ref. 10; Fig. 1A and B; Supplementary Fig. S1A; Supplementary Table S1). When present in PTCs, SWI/SNF gene mutations are subclonal, whereas they are clonal in PDTCs and ATCs, consistent with a role in tumor microevolution (Fig. 1C). As opposed to rhabdoid tumors, ovarian cancers, and renal clear cell carcinomas, where a specific SWI/SNF subunit gene is preferentially mutated, in PDTCs and ATCs there are nonoverlapping mutations of several components of BAF (*ARID1A, ARID1B*), PBAF (*ARID2*), or of *SMARCB1*, which is common to both complexes (Fig. 1D).

Arid1a, *Arid2*, or *Smarcb1* Loss Promotes Progression of Mouse Thyroid Cancers Driven by $Braf^{V600E}$

To determine the role of SWI/SNF loss in tumor progression, we generated mice with thyroid-specific homozygous loss of *Arid1a, Arid2*, or *Smarcb1*, either alone or in the context of a knock-in allele of $Braf^{V600E}$ (Fig. 2A). *TPO-Cre/Caggs-LSL-YFP/*$Arid1a^{fl/fl}$, *TPO-Cre/Caggs-LSL-YFP/*$Arid2^{fl/fl}$, and *TPO-Cre/Caggs-LSL-YFP/*$Smarcb1^{fl/fl}$ (hereafter *TA1a, TA2*, and *TSb1*) thyroids had no histologic changes through 20 weeks. Whereas *TPO-Cre/Caggs-LSL-YFP/LSL-*$Braf^{V600E}$ (*TBraf*) mice develop PTC by 5 weeks, *TBraf/A1a, TBraf/A2*, and *TBraf/Sb1* mice developed PDTC or ATC with short latency, characterized by a solid growth pattern, spindle cells, a high mitotic rate, and necrosis (Fig. 2B; Supplementary Fig. S2A and S2B). The $Arid1a^{fl/fl}$ locus was only partially recombined in *TA1a* mice, whereas in the *TBraf/A1a* recombination was almost complete. Accordingly, Western blots of cell lines generated from *TBraf/A1a, TBraf/A2 and TBraf/Sb1* tumors showed complete loss of the respective SWI/SNF subunit (Supplementary Fig. S3A). *TBraf/A1a* tumors had increased ARID1B expression (Supplementary Fig. S3B), consistent with evidence that ARID1B partially compensates for ARID1A loss and is synthetic lethal in ARID1A-deficient tumors (33). Human ATC with loss of SMARCB1 commonly show presence of rhabdoid cells consisting of large cells with eccentric nuclei and eosinophilic globular cytoplasm (Fig. 2C), which is morphologically similar to *SMARCB1*-mutant tumors of other lineages. *TBraf/Sb1* tumors phenocopy these features and exhibit vascular invasion and lymph node and lung metastasis (Fig. 2C). *TBraf/A1a* and *TBraf/Sb1* mice had decreased survival compared with *TBraf* animals (Fig. 2D). Whereas *TBraf* mice developed PTC, *TBraf/A1a* and *TBraf/Arid2* mice displayed tumor progression to PDTC or ATC, with a penetrance of 40% and 35%, respectively. Strikingly, loss of the core SWI/SNF subunit *Smarcb1* yielded a highly penetrant anaplastic transformation in 39 of 45 mice (87%; Fig. 2E).

SWI/SNF Loss Downregulates Thyroid Differentiation Gene Expression and Decreases Chromatin Accessibility at Key Thyroid Lineage Transcription Factors

SWI/SNF complexes support terminal differentiation (34), and their loss can promote stem cell–like properties and tissue regeneration (23, 35). FOXE1, NKX2-1, and PAX8 are key thyroid lineage TFs expressed in embryonic day E8.5–E10.5 during specification of the definitive endoderm (36). Loss of *Arid1a, Arid2*, or *Smarcb1* attenuated expression of thyroid lineage TFs, as well as of key genes involved in iodine organification in wild-type (WT) thyrocytes (Fig. 3A and B). Impairment of thyroid-differentiated gene expression in *TSb1* mice resulted in a compensatory increase in serum thyrotropin levels (Supplementary Fig. S4A).

To further investigate the impact of SWI/SNF loss on genome-wide chromatin accessibility, we performed Assay for Transposase-Accessible Chromatin using sequencing (ATAC-seq) on YFP-sorted *TA1a, TA2*, and *TSb1* thyroid cells. Loss of *Arid1a, Arid2*, or *Smarcb1* led to an overall decrease in chromatin accessibility compared with WT thyroid cells (Supplementary Fig. S4B). The majority of the dynamic peaks localized to intergenic regions or within introns (Supplementary Fig. S4C). ARID1A and SMARCB1 have been reported to maintain active enhancers that are primarily located within introns and intergenic regions (37–39). To compare the consequences of loss of the individual SWI/SNF subunits, we clustered all dynamic ATAC peaks from WT thyroid, *TA1a, TA2*, and *TSb1* cells.

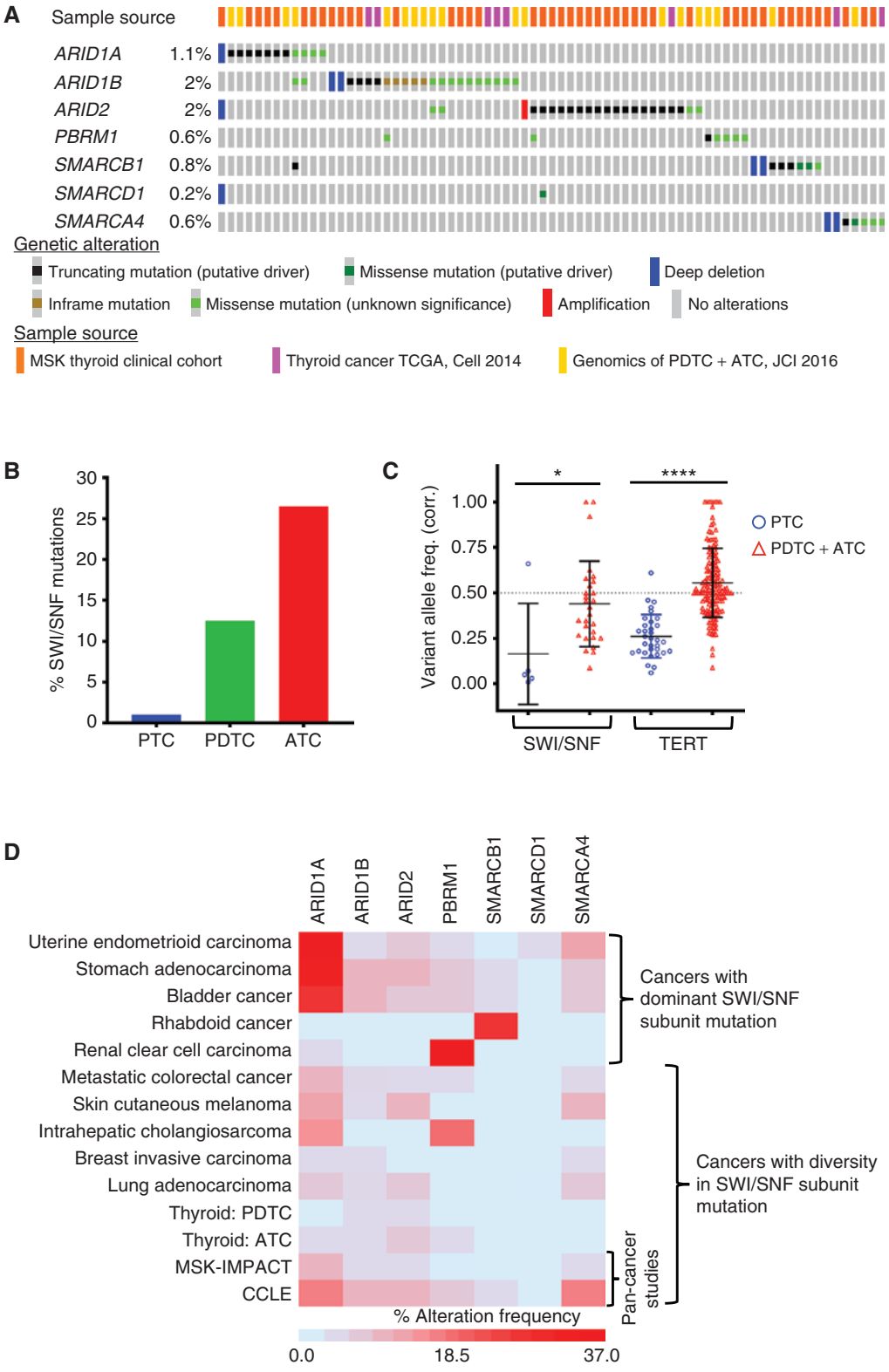

Figure 1. Mutations of SWI/SNF subunit genes are associated with thyroid tumor progression. **A,** Oncoprint of SWI/SNF subunit mutations in human thyroid cancers. The color-coded bars in the top row represent the data study source for each sample. Tissues from the MSK clinical cohort and from Landa et al. (10) were sequenced by MSK-IMPACT. The Cancer Genome Atlas (TCGA) genotyping was by whole-exome sequencing (9). **B,** Frequency of SWI/SNF mutations in human PTC, PDTC, and ATC. **C,** Clonality of SWI/SNF mutations in PTC vs. PDTC/ATC. Student *t* test, *, $P < 0.05$; ****, $P < 0.0001$. **D,** Frequency of SWI/SNF mutations in different cancer types. Unlike renal and rhabdoid cancers that predominantly harbor a distinct SWI/SNF subunit mutation, thyroid (ATC) and some other cancers have mutations in diverse SWI/SNF subunits.

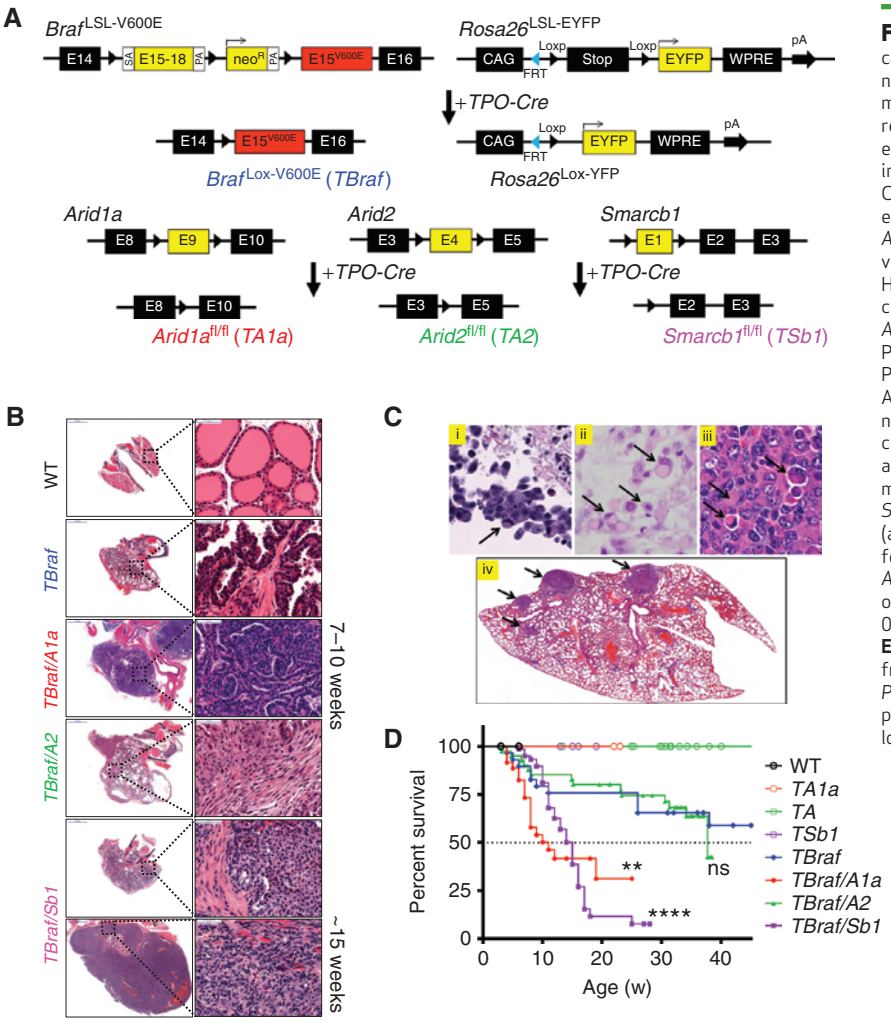

Figure 2. Modeling SWI/SNF loss in genetically engineered mouse models with endogenous $Braf^{V600E}$ expression. **A,** Schema of mouse models: Thyroid-specific expression of Cre recombinase driven by *TPO-Cre* substitutes exon 15 of WT *Braf* by a mutant allele, resulting in endogenous expression of $Braf^{V600E}$ (79). Cre-excision of stop cassette also enables YFP expression in thyroid cells. E9 of *Arid1a*, E4 of *Arid2*, and E1 of *Smarcb1* are floxed to inactivate the respective alleles. **B,** Representative H&E-stained thyroid sections of WT, *TBraf*, and compound *TBraf* mice with homozygous *A1a*, *A2*, or *Sb1* loss. *TBraf* mice develop classic PTC, whereas *TBraf/A1a* and *TBrafA2* have PDTC-like histology. *TBraf/Sb1* mice develop ATC at 15 weeks with spindle cells, irregular nuclei, and areas of necrosis. **C,** i–iv: Rhabdoid cells (arrows) in (i) human sinonasal carcinoma and (ii) human ATC with *SMARCB1* loss, and (iii) mouse *TBraf/Sb1* thyroid tumor. (iv) *TBraf/Sb1* mice exhibit frequent lung metastases (arrows). **D,** Kaplan–Meier survival analysis for mice with the indicated genotypes. *TBraf/A1a* and *TBraf/Sb1* mice had median survival of 11 and 15 weeks, with a log-rank *P* value of 0.0043 (**) and <0.0001 (****), respectively. **E,** Histologic classification of tumors obtained from mice with the indicated genotypes. *P* values for PTC vs. PDTC/ATC in *TBraf* vs. compound *TBraf* with homozygous *A1a*, *A2*, or *Sb1* loss were calculated using Fisher exact test.

E

		PTC	PDTC	ATC	*P* (PTC → PDTC/ATC)
TBraf	*n*	24	1	0	
	%	(96%)	(4%)	(0%)	
TBraf/A1a	*n*	21	13	1	0.0019
	%	(60%)	(37%)	(3%)	
TBraf/A2	*n*	13	2	5	0.0146
	%	(65%)	(10%)	(25%)	
TBraf/Sb1	*n*	6	0	39	<0.0001
	%	(13%)	(0%)	(87%)	

Unsupervised k-means clustering resolved the ATAC peaks into four clusters (Fig. 3C). We identified TF motifs enriched in the ATAC peaks in each cluster using HOMER *de novo* motif discovery (40). Cluster 1 showed enrichment of CTCF motifs in WT and *TSb1* cells (Fig. 3D), aligning with reports showing that loss of SMARCB1 promotes formation of a BRD9-containing noncanonical BAF complex, which localizes to CTCF sites (19, 41). BRD9 occupancy is enriched at motifs for the ETS family of TFs (42), consistent with increased accessibility at these sites in *TSb1* cells in clusters 2 and 4. Intersection of RNA sequencing (RNA-seq) and ATAC-seq revealed concordant changes for genes encoding lineage TF (ATAC down, RNA down) in all SWI/SNF knockout (KO) contexts compared with WT (Supplementary Fig. S5A–S5C).

There was a remarkable loss of accessibility to sites with DNA binding motifs of FOXE1, NKX2-1, and PAX8 in all SWI/SNF KO contexts (Fig. 3D and E). This was also true for NF1/CTF, which forms a complex with FOXE1, a pioneer TF of the thyroid lineage (43). Consistent with this, NF1/CTF and FOXE1 motifs co-occur at 29% of FOXE1 sites within peaks in cluster 3 (relative to the background distribution of FOXE1 motifs in nonaccessible sites; $P = 6.478e{-}09$, Fisher exact test). The integrated activity

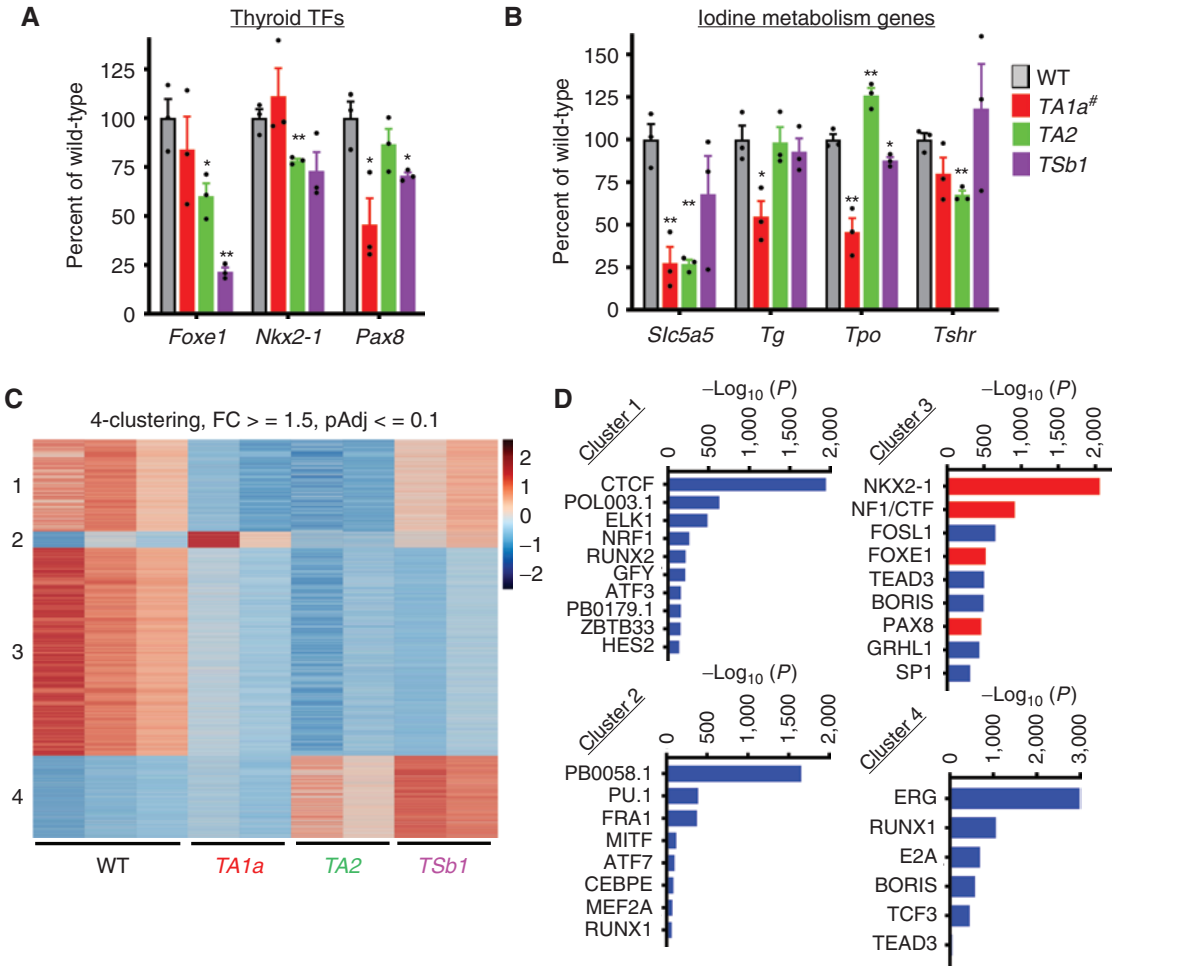

Figure 3. SWI/SNF loss downregulates expression and decreases chromatin accessibility of thyroid differentiation genes. **A** and **B,** Thyroid tissue lineage TF (**A**) and iodine metabolism (**B**) gene expression in homozygous *A1a, A2,* and *Sb1* knockout mice by RNA-seq as compared with WT. #Due to incomplete recombination of the floxed *Arid1a* allele in *TA1a* mice, RNA-seq was performed in YFP+-sorted compared with WT YFP+ cells ($n = 3$ per group; mean ± SEM; Student *t* test, *, P 0.05; **, $P \leq 0.01$ vs. WT). **C,** Unsupervised k-means clustering of ATAC-seq peak gains (red) and losses (blue) in the indicated genotypes ($n = 3$ biological replicates for WT, and 2 each per *TA1a, TA2,* and *TSb1*). Four groups are noted by unsupervised k-means clustering. **D,** TF motifs enriched in specific clusters identified using HOMER *de novo* motif discovery. Thyroid lineage TF motif enrichments are indicated as red bars in cluster 3. (*continued on next page*)

of these TFs is required for expression of genes regulating iodide transport, oxidation, incorporation into thyroglobulin, and thyroid hormonogenesis (27, 44–46). Loss of the individual SWI/SNF subunits consistently decreased accessibility to the entire set of genes involved in thyroid hormone biosynthesis (Fig. 3F). Example tracks of loci adjacent to *Foxe1, Pax8,* and *Slc5a5* (the gene encoding NIS, the sodium iodide symporter) show loss of peaks within gene bodies or putative enhancers in all SWI/SNF KO contexts (Fig. 3G). Interestingly, the far-upstream *Slc5a5* peak corresponds to a functionally characterized *Slc5a5* enhancer in rat and human thyroid cells (47).

Murine Thyroid Tumors with SWI/SNF Loss Are Resistant to the Redifferentiation Effects of MAPK Inhibition

Endogenous activation of $BRAF^{V600E}$ downregulates expression of thyroid TFs as well as genes involved in iodine metabolism (ref. 48; Supplementary Fig. S6A and S6B). Inhibition of MAPK signaling in thyroid cancers driven by oncogenic BRAF or RAS restores expression of thyroid differentiation genes in mice and in patients (30, 31). We asked whether the differentiation state of $BRAF^{V600E}$-driven tumors in the context of SWI/SNF gene deletions could also be restored by MAPK pathway blockade in the murine thyroid cancers (Fig. 4A). The expression of *Pax8, Nkx2-1,* and *Foxe1* is suppressed in *TBraf* mice and restored by treatment with the MEK inhibitor CH5126766 (CKI; refs. 30, 49). Loss of SMARCB1 renders *TBraf/Sb1* tumors refractory to the redifferentiation effects of CKI (Fig. 4B and C). Despite partial rescue of the lineage TFs in *TBraf/A1a* and *TBraf/A2* thyroid tissues by CKI, the expression of NIS, which is particularly critical for iodine uptake and thyroid hormonogenesis, was not restored (Fig. 4C).

We next asked whether the changes in gene expression resulting from treatment with CKI were associated with concordant effects on chromatin accessibility. The ATAC-seq dynamic peaks were resolved into seven clusters (Fig. 4D;

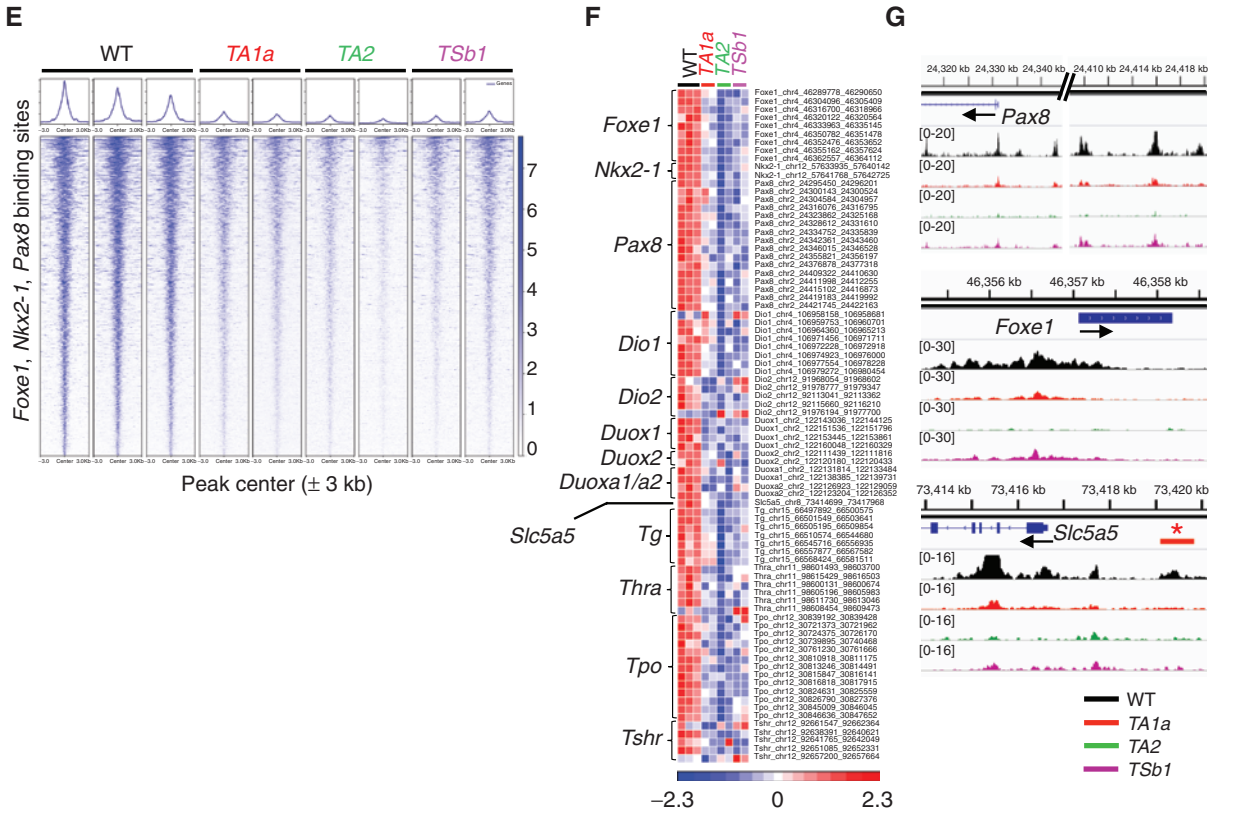

Figure 3. ***(Continued)*** **E,** Tornado plots of ATAC-seq signals representing 1,592 sites around the *Foxe1, Nkx2*-1, and *Pax8* binding sites sorted by $\log_2$ fold change (±3 kb of the peak center). **F,** Heat map of chromatin accessibility at the indicated thyroid differentiation genes. **G,** Representative Integrative Genomics Viewer (IGV) plots showing ATAC-seq peak losses at key thyroid lineage TFs: *Pax8 and Foxe1* at putative enhancer and promoter regions; *Slc5a5* proximal promoter and upstream enhancer elements (* marks confirmed *Slc5a5* enhancer; ref. 47).

Supplementary Fig. S7A). Associated genes per ATAC-seq cluster showed an expression profile consistent with that of the changing chromatin (Fig. 4E; Supplementary Table S2). We used HOMER motif analysis to identify TF motif enrichments in the seven ATAC clusters (Fig. 4F; Supplementary Fig. S7B). Accessibility to *Nf1/Ctf, Foxe1, Nkx2-1*, and *Pax8* binding motifs increased upon CKI treatment in *TBraf* cells, which was attenuated in *TBraf/A1a* and *TBraf/Sb1* cells (Fig. 4F, cluster 6 and Supplementary Fig. S8A). Conversely, peaks with ETS1 and JUN/AP1 motifs decreased upon CKI treatment in *TBraf* tumors, an effect that was dampened in *TBraf/A1a* and *TBraf/Sb1* cells (Supplementary Fig. S8B). ETS1 and JUN/AP1 motifs mark potential sites of regulation by MAPK, suggesting that *Arid1a* and *Smarcb1* loss may attenuate transcriptional responses to MAPK inhibition through effects distal to the phosphorylation state of canonical MAPK signaling effectors. Although CKI rescued expression of thyroid lineage TFs in *TBraf/A1a* cells, decreased accessibility to their respective DNA binding motifs likely impaired expression of key target genes (Fig. 4G; Supplementary Fig. S8A and S8C). Interestingly, treatment of *TBraf/A2* thyroid tumors with CKI restored expression of all three TFs and increased accessibility to their respective DNA binding motifs. However, this was insufficient to restore expression of NIS. Despite an increase in chromatin accessibility post-CKI in cluster 6 in *TBraf/A2* cells, the RNA-seq *z*-score of genes in this cluster post-CKI remained down, suggesting that disruption of other mechanisms, such as TF activity or histone modifications, may be implicated in this process. Overall, the majority of the top 50 differentially expressed genes upon CKI treatment had corresponding changes in chromatin accessibility in surrounding regulatory regions (Supplementary Fig. S9A).

Cluster 2 (*TBraf/A1a* and *TBraf/Sb1*) and cluster 5 (*TBraf/Sb1*) peaks were enriched for CTCF/BORIS motifs, suggesting that ncBAF maintains accessibility at these sites, and that this is insensitive to MAPK inhibition (Fig. 4F; Supplementary Fig. S10A).

Mouse Thyroid Tumor Cell Lines Fail to Recapitulate the Redifferentiation Effects of MAPK Inhibition *In Vivo*, but Display Consistent Epigenomic Vulnerabilities

We performed transcriptomic and epigenomic analyses in three independent cell lines derived from *TBraf, TBraf/A1a, TBraf/A2*, and *TBraf/Sb1* tumors, respectively, after incubation with CKI or vehicle for 8 days in the presence of bovine thyroid-stimulating hormone (TSH; Fig. 5A). By contrast to the effects of MAPK inhibition on *TBraf* tumor gene expression *in vivo* (Fig. 4B and C), treatment of *TBraf* cell lines with CKI leads to no appreciable increase in expression of *Foxe1* or of genes involved in iodine uptake and metabolism (*Nis*, *Tg*, *Tpo*, and *Tshr*; Fig. 5B and C). Accordingly, the increased chromatin accessibility at thyroid TF binding sites observed in response to CKI in *TBraf* tumors (Fig. 4D) was not recapitulated *in vitro* (see Fig. 5D,

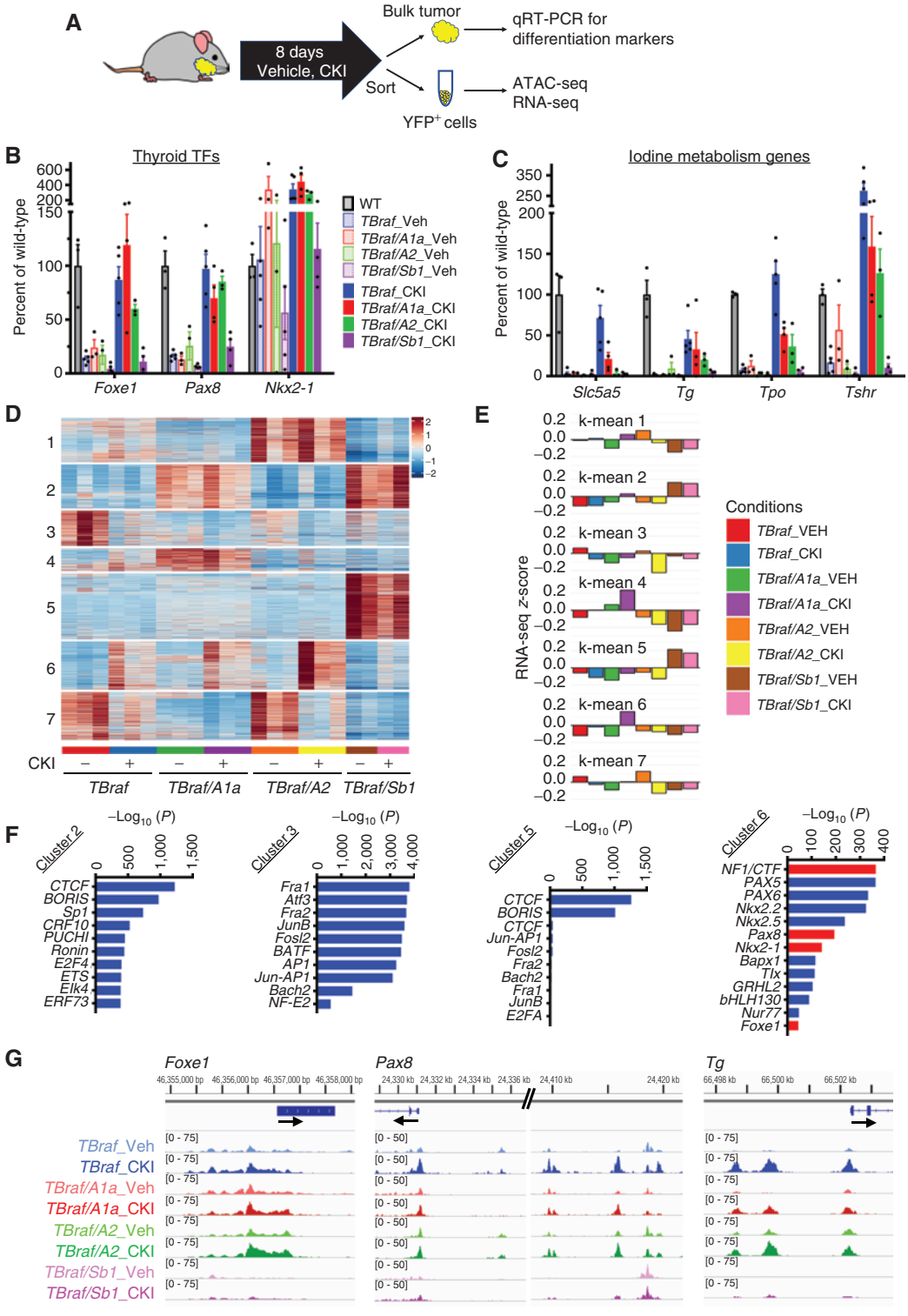

Figure 4. *Braf*-mutant thyroid tumors with SWI/SNF loss are refractory to the redifferentiation effects of MEK inhibition. **A,** Mice were treated with the MEK inhibitor CKI for 8 days, and bulk thyroids collected for qRT-PCR of thyroid differentiation markers or disaggregated and YFP-sorted for ATAC-seq and RNA-seq profiling. **B** and **C,** Quantitative RT-PCR of (**B**) lineage TFs and of (**C**) iodine metabolism genes ($n \geq 3$/group; mean ± SEM). **D,** Unsupervised k-means clustering analysis of differential ATAC-seq peaks of YFP-sorted thyroid tumors treated with or without CKI ($n = 3$ for vehicle and CKI-treated *TBraf*, *TBraf/A1a*, *TBraf/A2*; $n = 2$ for *TBraf/Sb1*). **E,** RNA-seq mean *z*-score of the genes present in each of the seven ATAC-seq k-means clusters (*P* values for ATAC-seq to RNA-seq concordance are shown in Supplementary Table S2). **F,** TF motifs enriched in clusters 2, 3, 5, and 6 identified using known sequence motifs curated by the HOMER suite. Thyroid lineage TF motif enrichments are indicated as red bars in cluster 6. TF motif enrichments for clusters 1, 4, and 7 are shown in Supplementary Fig. S7B. **G,** ATAC-seq IGV plots of the indicated genotypes treated with or without CKI.

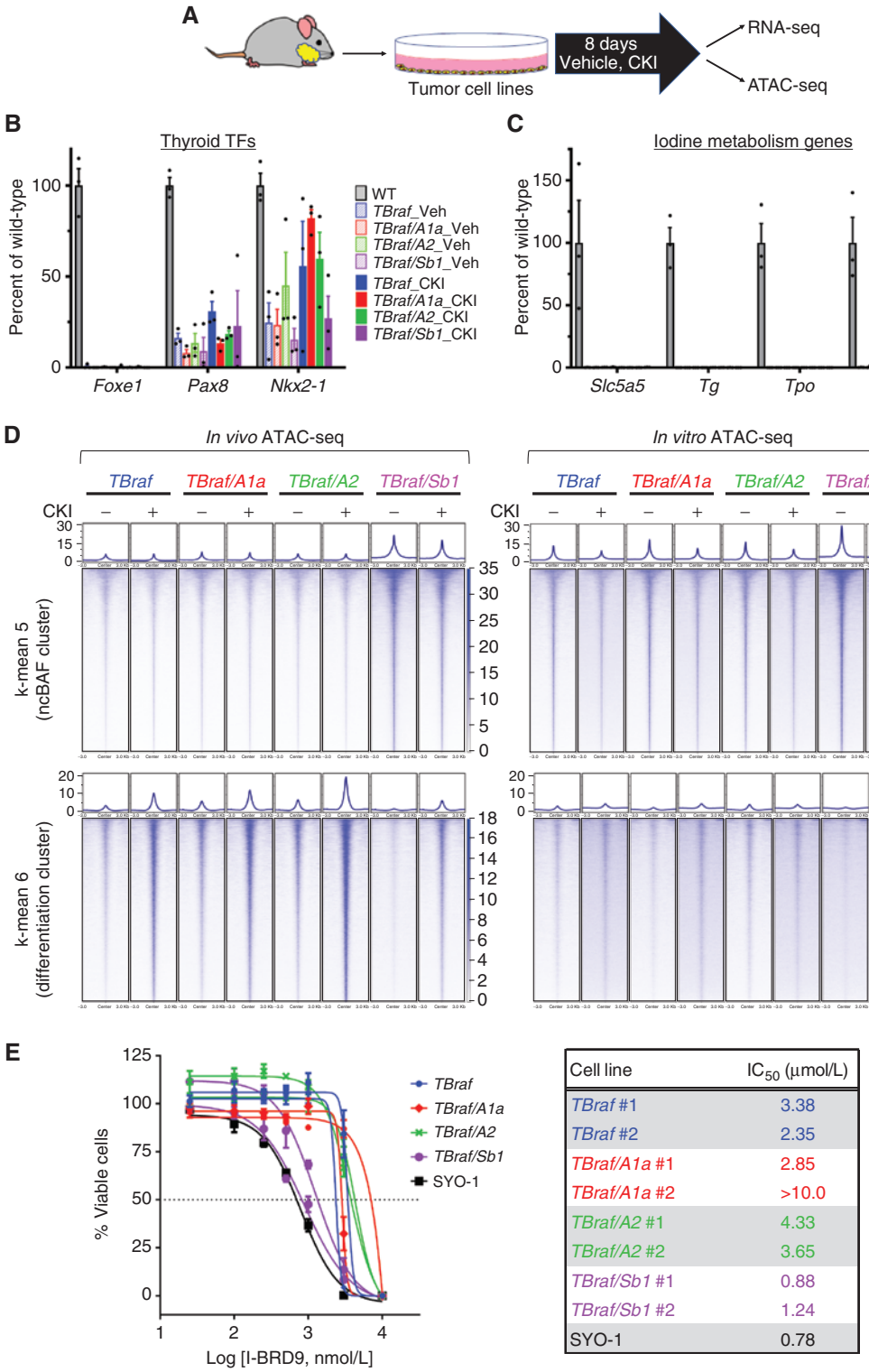

Cell line	IC_{50} (μmol/L)
TBraf #1	3.38
TBraf #2	2.35
TBraf/A1a #1	2.85
TBraf/A1a #2	>10.0
TBraf/A2 #1	4.33
TBraf/A2 #2	3.65
TBraf/Sb1 #1	0.88
TBraf/Sb1 #2	1.24
SYO-1	0.78

Figure 5. Response of mouse thyroid cancer cell lines to MAPK and BRD9 inhibitors. **A,** Three thyroid tumor cell lines derived from each of the mouse genotypes were treated with 300 nmol/L CKI for 8 days in the presence of bovine TSH, after which cells were harvested for RNA-seq or ATAC-seq. **B** and **C,** Expression of (**B**) thyroid lineage TFs and (**C**) iodine metabolism genes in *TBraf*, *TBraf/A1a*, *TBraf/A2*, and *TBraf/Sb1* cell lines compared with normal thyroid tissue (each dot represents an independent thyroid tumor cell line; $n = 3$; mean ± SEM). **D,** Tornado plots of averaged ATAC-seq signals ±3 kb of peak center in cell lines treated with or without CKI for genes in cluster 5 (top right, 17,157 sites) and cluster 6 (bottom right, 12,618 sites) compared with the ATAC-seq signals *in vivo* (top left and bottom left for clusters 5 and 6, respectively). **E,** CellTiter-Glo cell viability assay in the indicated panel of cell lines treated with BRD9 bromodomain inhibitor I-BRD9 for 6 days ($n = 3$, mean ± SD); IC_{50} values are shown on the right.

cluster 6: "differentiation cluster"). *TBraf/A1a, TBraf/A2*, and *TBraf/Sb1* cell lines were uniformly dedifferentiated and unresponsive to CKI.

Whereas the cell lines proved inadequate to study thyroid redifferentiation, we found that *TBraf/Sb1* cell lines retained the increased accessibility at CTCF motifs observed *in vivo* (Fig. 5D). Upon SMARCB1 loss, SWI/SNF complex subunits reassemble into BRD9-containing ncBAF complexes that bind to active enhancers and active promoter regions enriched for CTCF motifs (41, 42). Chromatin immunoprecipitation sequencing (ChIP-seq) of the murine thyroid tumor cell lines showed strong enrichment of H3K4me1 (active enhancer), H3K4me3 (active promoter), and H3K27ac (active promoter and enhancer) marks in the CTCF-enriched cluster 5 in *TBraf/Sb1* cells (Supplementary Fig. S11A and S11B). To test whether *TBraf/Sb1* cells are dependent on the ncBAF complex for survival, we treated cells with the BRD9 inhibitor I-BRD9 (50). BRD9 is a subunit of ncBAF, and its inhibition is synthetic lethal upon SMARCB1 loss in malignant rhabdoid and synovial sarcoma cell lines (41, 42, 51). Similar to the synovial sarcoma cell line SYO-1, which shows synthetic lethality to I-BRD9 (51), *TBraf/Sb1* cell lines were sensitized to I-BRD9 treatment as compared with the other cell line genotypes (Fig. 5E).

Loss of SWI/SNF Subunits Promotes Refractoriness to RAI Uptake upon Treatment with MEK Inhibitor in Mice

Expression of genes required for iodide transport and organification into thyroglobulin is central to the ability of thyroid cancers to respond to RAI therapy. There is an inverse relationship between the transcriptional output of MAPK and the expression of thyroid differentiation genes in PTC (9). Accordingly, RAF or MEK inhibitors restore RAI uptake in mice and humans with RAI-refractory *BRAF*- or *RAS*-mutant differentiated thyroid cancers (30, 31). As previously reported, CKI increased ^{124}I uptake in *TBraf* mice (30), which was attenuated in *TBraf/A1* and *TBraf/Sb1* tumors, and to a lesser extent in *TBraf/A2* mice (Fig. 6A and B). Whereas treatment with CKI profoundly inhibited ERK phosphorylation in *TBraf* and *Braf-Swi/Snf* KO mice, it failed to restore membrane NIS expression following SWI/SNF loss (Fig. 6C and D; Supplementary Fig. S12A and S12B).

Loss of *ARID1A, ARID2*, or *SMARCB1* Is Associated with Resistance to MAPK Inhibition–Based Redifferentiation Therapy and RAI Uptake in a Limited Data Set of Human Thyroid Cancers

The MEK inhibitor selumetinib restored RAI responsiveness in patients with RAI-refractory *RAS*-mutant cancers, whereas *BRAF*^{V600E}-driven tumors had an attenuated response (31). *BRAF*-mutated thyroid cancers exhibit adaptive resistance to RAF inhibitors driven by neuregulin-dependent HER3/HER2 activation (52). Based on this, we designed a pilot study of vemurafenib in combination with the HER3 targeting antibody CDX-3379 (NCT02456701) for BRAF-mutant RAI-refractory metastatic thyroid cancer, focusing on their combined effects on redifferentiation and response to RAI therapy (Supplementary Fig. S13A). ^{124}I uptake was markedly increased by this combination in a representative patient with lung metastases (Fig. 7A). By contrast, a patient harboring a *BRAF*-mutant tumor with biallelic truncation mutations of *ARID2* failed to show clinically significant restoration of RAI incorporation on this treatment. RNA-seq of serial lesional biopsies of these two patients (prior to treatment, on vemurafenib, and on vemurafenib + CDX-3379) showed restoration of the thyroid differentiation score (9, 53) in the *BRAF*–SWI–SNF WT compared with the *BRAF*–*ARID2*-mutant metastases (Fig. 7B). The MAPK pathway transcriptional output (54) was inhibited by vemurafenib and vemurafenib + CDX-3379 in the index metastases of both these patients.

We also explored the impact of SWI/SNF mutations in a phase II redifferentiation trial of trametinib for patients with *RAS*-mutant RAI-refractory thyroid cancer (NCT02152995; Supplementary Fig. S13B). Out of 25 patients, two harbored *SMARCB1* and one an *ARID1A* mutation (Supplementary Fig. S13C). None of these three patients showed clinically significant restoration of iodine uptake in response to the MEK inhibitor. ^{124}I PET-CT scans of these patients and of a representative *RAS*-mutant responder are shown in Fig. 7C.

DISCUSSION

Soon after the discovery of BRAF^{V600E} mutations in PTC, these tumors were found to exhibit a greater decrease in expression of iodine metabolism genes as compared with BRAF-negative PTCs (55) and to be disproportionately refractory to RAI therapy (56). BRAF^{V600E} signals as a monomer and is unresponsive to negative feedback of pERK on RAF dimers, and consequently has a higher MAPK signaling output than that induced by fusion RTKs or mutant RAS (57). There is a tight inverse relationship between the intensity of the MAPK signaling flux, as measured by its integrated transcriptional output (54), and the expression of thyroid differentiation genes (58). This reciprocal relationship is causal, as shown following the conditional activation and silencing of BRAF^{V600E} in thyroid cells *in vivo* (29). The mechanisms that account for this interaction are complex, but are rooted in inhibitory effects of pERK on key nodes of the cAMP signaling pathway, which mediates TSH-stimulated expression of iodide-metabolizing genes (59–61). In addition, constitutive MAPK activation interferes with the transcriptional activities of NKX2-1 and PAX8 (62, 63). Here we show that endogenous expression levels of BRAF^{V600E} almost completely silence expression of the three thyroid lineage TFs *in vivo*. This is associated with decreased chromatin accessibility at multiple sites adjacent to or within these genes, all of which are restored by treatment with the MEK inhibitor CKI (Fig. 7D). This is also true across the entire differentiation gene cluster. Following treatment with CKI, there was also a marked increase in accessibility at peaks with binding motifs for the three thyroid TFs, with the binding sites for NF1/CTF, a TF that forms a complex with FOXE1, being the most highly represented. FOXE1 is a pioneer TF in thyroid follicular cells (64). The increase in FOXE1 by MAPK pathway blockade may play a central role in driving the overall gains of chromatin accessibility in the differentiation gene cluster, although this has not been tested experimentally.

Deletion of *Arid1a, Arid2*, or *Smarcb1* in thyroid follicular cells did not cause an overt phenotype. There was no

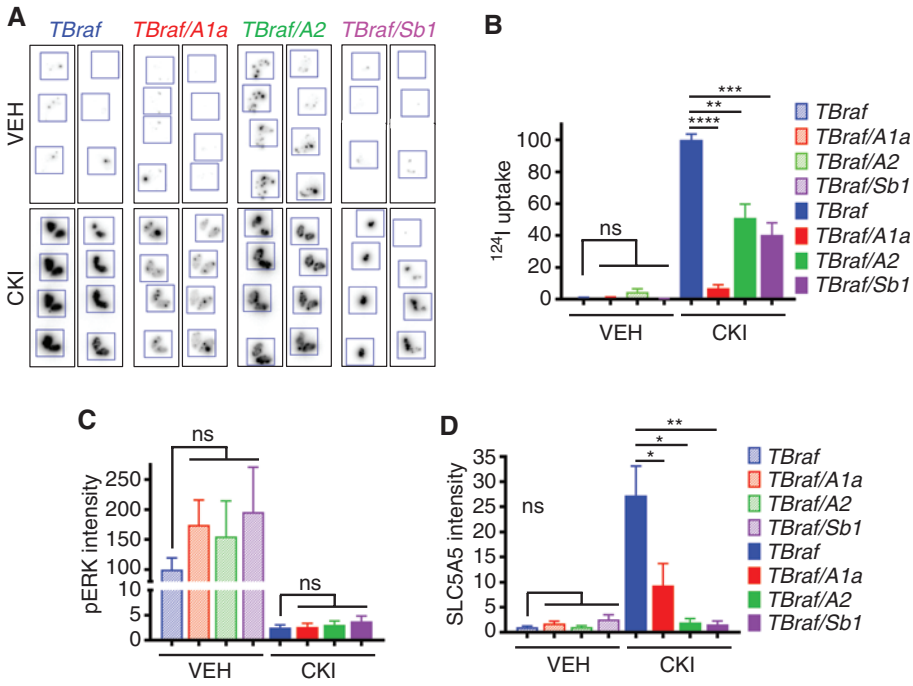

Figure 6. SWI/SNF loss prevents restoration of RAI uptake by the MEK inhibitor CKI. **A,** Representative autoradiograms of thyroid cancer tissue sections of mice with the indicated genotypes treated with or without CKI for 8 days. At day 5, they received 70 μCi of ^{124}I by gavage. **B,** ^{124}I uptake quantified using ImageJ. **C** and **D,** Quantification of immunofluorescence staining for pERK (**C**) and SLC5A5 (**D**). $n \geq 3$; mean ± SEM. *, $P \leq 0.05$; **, $P \leq 0.01$; ***, $P \leq 0.001$; ****, $P \leq 0.0001$; Student *t* test.

difference in mouse weight or longevity through one year of life, or histologic abnormalities in the thyroid. This needs to be reconciled with the attenuated expression of the lineage TFs and the iodide metabolizing genes, and the decreased chromatin accessibility at those sites. Inactivation of the SWI/SNF genes in these mouse models took place through Cre recombinase expression beginning at E14.5, a time when thyroid organogenesis has already taken place (65). The mitotic rate and overall turnover of thyroid follicular cells in late gestation and throughout postnatal life is very low (66). This suggests that integrity of SWI/SNF complexes may not be required for maintenance of the thyroid differentiated state. This is particularly noteworthy in the setting of *Smarcb1* loss, which disrupts both the BAF and PBAF complexes. *TSb1* mice did, however, have a modest increase in TSH levels, consistent with a state of compensated hypothyroidism.

The increase in chromatin accessibility at FOXE1, NKX2-1, and PAX8 binding sites post-CKI was dampened in *TBraf/A1a* and *TBraf/Sb1* tumor cells, which was associated with impaired expression of their target genes. Curiously, this was not the case for *TBraf/A2* tumor cells. Disruption of the PBAF complex by loss of *Arid2* did not blunt the restoration of lineage TF expression by CKI, or chromatin accessibility to their binding sites. Despite this, NIS, the plasma membrane symporter required for iodide uptake (67), was not restored by CKI. Inspection of the ATAC-seq Integrative Genomics Viewer (IGV) plots did show shallower peaks at the *Nis* gene following CKI in *TBraf/A2* as compared with *TBraf* cells. The attenuated NIS expression upon *Arid2* loss could in part also be mediated by secondary effects, such as histone modifications or mRNA stability.

Difficulties in obtaining a high enough yield of YFP-labeled thyroid cells from thyroid tumors *in vivo* precluded our ability to do ChIP-seq analyses to study the SWI/SNF and histone modifications that likely mediate the dynamic changes in chromatin accessibility seen upon MAPK inhibition. Moreover, BRAF^{V600E}-mutant tumor cell lines derived from mouse tumors fail to recapitulate the restoration of thyroid differentiated gene expression seen upon MAPK inhibition *in vivo*. This may require development of new *in vitro* models that allow cells to maintain cell polarity, which is critical for most normal thyrocyte functions, and/or the presence of other cell types.

Whereas mouse thyroid tumor cell lines were inadequate to study thyroid redifferentiation, the epigenomic vulnerability created by SMARCB1 loss was conserved. *TBraf/Sb1* cell lines had increased chromatin accessibility at CTCF/BORIS motifs, which were decorated with active enhancer/promoter histone marks. Like rhabdoid and synovial cancer cells with SMARCB1 loss, *TBraf/Sb1* cell lines were sensitized to BRD9 inhibition, indicating that the dependency on ncBAF occurs across tumor lineages. Mutations in SWI/SNF complexes also create a dependency on the PRC2 complex, which manifests in synthetic lethality when the activity of its EZH2 methyltransferase subunit is inhibited (24, 25). However, activation of the RAS pathway has been shown to abrogate this dependency (68). Whether this also applies to BRAF-driven thyroid cancers remains to be tested, as well as whether the EZH2 dependency for viability in SWI/SNF-mutant cells can be rescued by MAPK pathway blockade.

Aside from the impact of SWI/SNF loss on the differentiation state of thyroid cancer and on its plasticity in response to MAPK pathway inhibition, deletion of *Arid1a* or *Smarcb1* promoted progression to more advanced forms of the disease, and in the case of *Smarcb1* to a high penetrance of distant metastases. This is consistent with data from a forward genetic screen for lesions that cooperate with oncogenic RAS in tumor progression, which identified chromatin modifiers as the dominant class (16), and from the relative frequency of SWI/SNF mutations in human PDTC and ATC as compared with PTCs.

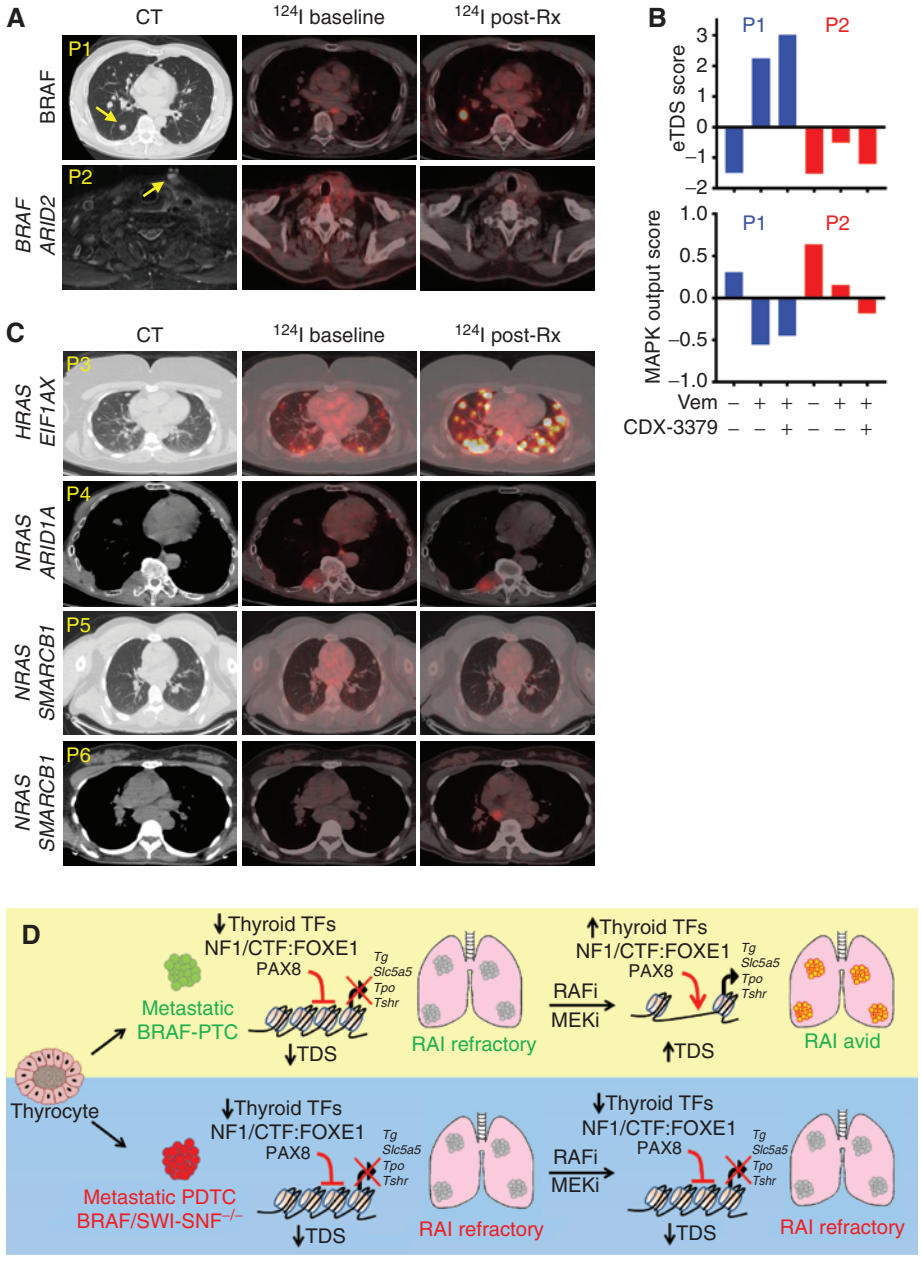

Figure 7. Thyroid cancers with *ARID1A*, *ARID2*, or *SMARCB1* mutations are resistant to redifferentiation by MAPK pathway inhibitors. **A,** Axial CT (left) and fused ^{124}I-PET-CT chest images (middle and right) of two patients with thyroid cancer (P1 and P2) with RAI-refractory metastatic thyroid cancer treated for 4 weeks with vemurafenib (Vem) combined with the HER3 monoclonal antibody CDX-3379. Baseline ^{124}I-PET-CT was performed prior to drug exposure; on Rx ^{124}I-PET-CT was done while on the drug combination. P1 harbored a BRAF^{V600E}-mutant tall cell variant PTC and showed restoration of ^{124}I uptake in previously negative metastatic lesions. P2 harbored a *BRAF* and *ARID2*-mutant PDTC that failed to incorporate ^{124}I after Vem + CDX-3379. **B,** Enhanced thyroid differentiation score (eTDS) and MAPK output scores in RNA-seq of three serial biopsies of the index lesions (arrows) in P1 (responder) and P2 (nonresponder). Bars represent the eTDS and MAPK scores prior to treatment, on vemurafenib alone, and after adding CDX-3379. **C,** Axial CT and fused ^{124}I-PET-CT chest images of patients enrolled in a redifferentiation trial with the MEK inhibitor trametinib. P3 harbored a *RAS*-mutant PTC that showed restoration of ^{124}I uptake with trametinib, whereas patients P4 (*RAS* + *ARID1A*), P5 and P6 (*RAS* + *SMARCB1*) failed to enhance ^{124}I uptake on trametinib. **D,** Model depicting loss of chromatin accessibility at thyroid lineage genes and resistance to MAPK inhibitor–based redifferentiation in BRAF^{V600E}-mutant thyroid cancers with SWI/SNF loss.

SWI/SNF mutations have also been reported to favor metastatic spread in breast and hepatocellular carcinomas (69, 70).

TBraf/A1a, *TBraf/A2*, and *TBraf/Sb1* mice had significantly attenuated ^{124}I uptake post-CKI as compared with *TBraf* tumors. A recent series of pilot clinical trials have shown that a short course of treatment with RAF or MEK inhibitors can restore RAI responsiveness in a subset of patients with *RTK* fusion-, *BRAF*-, or *RAS*-mutant RAI-refractory thyroid cancer (31, 32, 53). Among patients treated at our institution, the few whose tumors harbored SWI/SNF mutations consistently failed to redifferentiate in response to MAPK pathway inhibition. BRAF^{V600E}-mutant thyroid cancers develop adaptive resistance to RAF kinase inhibitors through activation of neuregulin-driven HER3/HER2 signaling (52). One patient enrolled in an ongoing small pilot redifferentiation trial of a combination of vemurafenib with the HER3 monoclonal antibody CDX-3379, given sequentially, harbored biallelic truncation mutations of *ARID2*. An index metastatic lesion was serially biopsied throughout the study, allowing analysis of the transcriptomic changes in response to the drugs. Despite strong suppression of the MAPK transcriptional output, there was no increase in the thyroid differentiation score (TDS) or in the lesional ^{124}I uptake, whereas a comparator patient without SWI/SNF alterations showed a robust restoration of TDS and lesional ^{124}I incorporation. Similarly, 3 of 25 patients enrolled in a redifferentiation trial with the MEK inhibitor trametinib for *RAS*-mutant metastatic RAI-refractory thyroid cancers harbored mutations of SWI/SNF genes, and all failed to increase lesional ^{124}I uptake in the metastases while on the drug. These case examples do not

conclusively demonstrate that deleterious mutations of these SWI/SNF complex genes render patients irreversibly RAI-refractory, which would require a much larger patient cohort. Instead, they represent a signal pointing to the plausibility of this effect. In the context of our mouse data, they lend credibility to the premise that loss of function of these SWI/SNF subunits locks thyroid cancer cells with constitutively activated MAPK signaling into a dedifferentiated state that cannot be reprogrammed by inhibitors of the pathway.

The effects of SWI/SNF complex gene mutations on differentiation have also been seen in other therapeutically relevant disease contexts. Loss of *ARID1A* in estrogen receptor–positive (ER^+) breast cancer cells promotes resistance to ER antagonists by facilitating a switch from luminal to ER-independent basal-like cells (71, 72). In the setting of thyroid cancer, presence of deleterious SWI/SNF subunit lesions may prompt physicians to consider treatment alternatives other than RAI, as the toxicities of RAI cannot be disregarded (73–75). There is a compelling need to identify patients most likely to benefit from treatments requiring high administered activities of ^{131}I, as opposed to the current practice of empirically treating patients with this radioisotope irrespective of tumor genotype.

METHODS

Thyroid Cancer Genotyping

Somatic mutation frequency of the indicated genes in PTCs was obtained from The Cancer Genome Atlas (9). Somatic mutations of SWI/SNF complex encoding genes in PDTC and ATC were obtained from Landa and colleagues (10) as well as from a Memorial Sloan Kettering (MSK) clinical cohort profiled using the MSK-IMPACT (Integrated Mutation Profiling of Actionable Cancer Targets) assay. This assay involves hybridization of barcoded libraries to custom oligonucleotides (Nimblegen SeqCap) designed to capture all protein-coding exons and select introns of commonly implicated oncogenes, tumor suppressor genes, and members of pathways deemed actionable by targeted therapies. Libraries were prepared using 100–200 ng genomic DNA with the KAPA Hyper Prep Kit (Kapa Biosystems KK8504) and combined in a single equimolar pool. The captured pool was subsequently sequenced on an Illumina HiSeq 2500 or HiSeq 4000 as paired-end 100-base pair reads, producing an average of 849-fold coverage per tumor. Oncoprints of the SWI/SNF mutations in patients with thyroid cancer, lollipop plots, as well as frequencies of SWI/SNF subunit mutations were obtained from the cBioPortal for Cancer Genomics (http://www.cbioportal.org; ref. 76).

Clonality of the SWI/SNF and *TERT* mutations was calculated by correcting the allelic frequency of the mutations for tumor purity, which was assessed using the allele frequency of *BRAF* or *RAS* mutations (heterozygous *BRAF* or *RAS* mutations are considered clonal; ref. 10). Tumors with *BRAF* or *RAS* allele frequency <0.05 (<10% tumor purity) were excluded from the analysis.

Generation of Thyroid-Specific Arid1a, Arid2, Smarcb1 KO Mice

All animals used in this study were maintained on a mixed strain background. Animal care and all experimental procedures were approved by the MSKCC Institutional Animal Care and Use Committee. *TPO-Cre* mice obtained from Dr. Shioko Kimura (NCI; ref. 65) were bred to LSL-EYFP mice purchased from The Jackson Laboratory (stock number 007903) to generate the *TPO-Cre/EYFP (TE)* line. *FRT-lacZ-neo/Arid2*$^{fl/+}$ mice purchased from Mutant Mouse Resource and Research Centers (MMRRC; stock number 036982-UNC) were bred to *β-actin-Flpe* mice (The Jackson Laboratory; stock number 003800) to generate *Arid2*$^{fl/+}$ mice, and the littermates were interbred to breed out *β-actin-Flpe* and generate *Arid2*$^{fl/fl}$ mice. *Arid1a*$^{fl/fl}$ (obtained from Dr. Zhong Wang; ref. 77), *Arid2*$^{fl/fl}$, and *Smarcb1*$^{fl/fl}$ mice (obtained from Dr. Charles W.M. Roberts; ref. 78) were then bred to the *TE* line to generate *TE/Arid1a*$^{fl/fl}$ (*TA1a*), *TE/Arid2*$^{fl/fl}$ (*TA2*), and *TE/Smarcb1*$^{fl/fl}$ (*TSb1*) mice. Expression of Cre recombinase at E14.5 days under the control of the thyroid-specific *TPO* promoter results in expression of YFP, as well as deletion of exon 9 in *Arid1a*, exon 4 in *Arid2*, or exon 1 in *Smarcb1*, respectively. To study the role of SWI/SNF loss in the context of $BRAF^{V600E}$, *Arid1a*$^{fl/fl}$, *Arid2*$^{fl/fl}$, and *Smarcb1*$^{fl/fl}$ mice were bred to *LSL-Braf*$^{V600E/+}$ (79) mice, and the resulting *Braf*$^{V600E/+}$*/Arid1a*$^{fl/fl}$, *Braf*$^{V600E/+}$*/Arid2*$^{fl/fl}$, and *Braf*$^{V600E/+}$*/Smarcb1*$^{fl/fl}$ mice were bred to *TA1a, TA2*, and *TSb1* mice, respectively, to generate the following lines: *TE/Braf*$^{V600E/+}$*/Arid1a*$^{fl/fl}$ (*TBraf/A1a*), *TE/Braf*$^{V600E/+}$*/Arid2*$^{fl/fl}$ (*TBraf/A2*), and *TE/Braf*$^{V600E/+}$*/Smarcb1*$^{fl/fl}$ (*TBraf/Sb1*). Toe clips were submitted to Transnetyx for genotyping.

For survival analysis, mice were monitored for health and euthanized because of tumor burden upon recommendation by the Research Animal Resource Center (RARC) veterinary staff. For *in vivo* treatments, mice were randomized into treatment with vehicle (40% Trappsol, Cyclo Therapeutics) or CH5126766 (CKI) 1.5 mg/kg (Chugai Pharmaceutical) once a day by gavage for eight days. Mice were euthanized, and blood and thyroid tumors were harvested ~2 hours after the last dose.

^{124}I Autoradiography

Mice were treated with vehicle or CKI for 8 days, and at day five 70 μCi of ^{124}I was administered by oral gavage. Three days after the ^{124}I administration, mice were euthanized and thyroid tumors dissected and embedded in optimal cutting temperature blocks. Three to four 10-μm-thick cryosections of each tumor ~250 μm apart were obtained and affixed to a glass slide. Slides were exposed to a phosphor screen for 24 hours prior to scanning with a Typhoon FLA 7000 scanner. The autoradiogram was analyzed using ImageJ.

Ultrasonic Imaging

Mice were anesthetized by inhalation with isofluorane (Henry Schein) with 1% O_2. Thyroid tumors were imaged using Vevo 770 High-Resolution *In Vivo* Micro-Imaging System (VisualSonics). Aqueous ultrasonic gel was applied to the denuded skin overlying the thyroid gland prior to placement of the ultrasonic transducer. Volume was calculated by manually tracing the margin of the tumor every 250 μm using the instrument software.

TSH Assay

Blood from mice was collected immediately after euthanasia with CO_2 and centrifuged at maximum speed at 4°C for 15 minutes, and serum was removed and stored at −70°C until assayed. Serum TSH levels were determined as previously described (80). The lower limit of detection for TSH in this assay is 10 mU/L.

Histology and IHC

Paraformaldehyde (PFA)-fixed paraffin-embedded thyroid tissues were sectioned, stained with hematoxylin and eosin (H&E), and graded by a pathologist blinded to mouse genotype. For immunofluorescence staining, sections were deparaffinized, blocked, and permeabilized with 1% BSA and 0.1% Triton X 100, and stained with antibodies for Ki-67 (Abcam; cat. #ab15580), pERK (Cell Signaling Technology; cat. #4370,) and rabbit anti-Rat SLC5A5 (kindly provided by Dr. Nancy Carrasco, Vanderbilt School of Medicine), followed by biotinylated goat anti-rabbit secondary antibody (1:200; Vector Laboratories; catalog no. PK-6101). The biotinylated secondary antibody was detected using Alexa Fluor 647 Tyramide reagent (Invitrogen; catalog no. B40958). Slides were scanned with Pannoramic P250 Flash scanner (3-DHistech) using 20×/0.8NA objective lens. Regions of interest around the tissues were then drawn and

exported as .tif files using Caseviewer (3-DHistech). Images were analyzed using ImageJ/FIJI where a median filter, thresholding, and water shedding were used to segment the nuclei in the DAPI channel. Thresholding in A647 channel was then used to determine the fluorescence intensity.

Flow Cytometry

To isolate YFP$^+$ thyroid cells for transcriptomic and epigenomic characterization, tumor and WT thyroids were harvested in cold minimal essential medium (MEM), minced in dissociation buffer (Collagenase A 0.42 mg/mL; Dispase 1.1 mg/mL in MEM), and incubated at 37°C for 1 hour with intermittent vortexing every 10 minutes. Dissociated thyroid cells were collected by centrifugation at 500 × *g* for 5 minutes, and the pellet washed and resuspended in cold F-12 Coon media containing 5% FBS, 0.5% bovine brain extract, 100 U/mL penicillin, and 0.1 mg/mL streptomycin (Complete Medium). The cells were passed through a 40-μm mesh, and the YFP$^+$ pure thyroid cell population sorted using a BD FACSAria flow cytometer into TRIzol LS (Invitrogen, #10296010) for RNA-seq or Complete Medium for ATAC-seq. Thyroids pooled from approximately 15 non-BRAF mice (*WT, TA1a, TA2*, and *TSb1*) or three tumor-bearing mice in the various BRAF contexts were used to generate individual replicates for ATAC-seq and/or SMARTer Amp RNA-seq.

RNA-seq of Mouse Thyroid Cells

Total RNA was isolated from ~20,000 YFP$^+$ cells sorted into TRIzol LS reagent. Phase separation in cells lysed in TRIzol reagent was induced with chloroform. RNA was precipitated with isopropanol and linear acrylamide and washed with 75% ethanol. The samples were resuspended in RNase-free water. After RiboGreen quantification and quality control by Agilent BioAnalyzer, 1–2 ng total RNA with RNA integrity numbers ranging from 7.5 to 10 underwent amplification using the SMART-Seq v4 Ultra Low Input RNA Kit (Clonetech; catalog no. 63488), with 12 cycles of amplification. Subsequently, 9.2–10 ng of amplified cDNA was used to prepare libraries with the KAPA Hyper Prep Kit (Kapa Biosystems KK8504) using eight cycles of PCR. Samples were barcoded and run on a HiSeq 4000 in a 50 bp/50 bp paired-end run, using the HiSeq 3000/4000 SBS Kit (Illumina). An average of 48 million paired reads were generated per sample, and the percentage of mRNA bases per sample ranged from 57% to 81%.

Raw reads were 3′ trimmed for quality (threshold of 15) and adapter sequences using version 0.4.5 of TrimGalore (https://www.bioinformatics.babraham.ac.uk/projects/trim_galore), and then aligned to mouse assembly mm9 with STAR v2.4 (81) using default parameters. Post-alignment quality and transcript coverage were assessed using the Picard tool CollectRNASeqMetrics (http://broadinstitute.github.io/picard/). Raw read count tables were created using HTSeq v0.9.1 (82). Normalization and expression dynamics were conducted with DESeq2 (83) using the default parameters including library size factor normalization.

ATAC-seq

YFP-sorted cells (50,000) from tissues or cell lines were lysed in 50 μL lysis buffer (84) and subjected to transposition with Nextera Tn5 transposase according to the manufacturer's instructions (Illumina FC-121–1030). DNA was eluted from a MinElute column in 11.5 μL elution buffer (Qiagen). ATAC libraries were constructed using the NEBNext High-Fidelity 2× PCR Master Mix (NEB M0541) as in Buenrostro and colleagues (84) with the following modifications: DNA was PCR-amplified for 1 cycle of 5 minutes at 72°C and 30 minutes at 98°C followed by 12 cycles of 10 minutes at 98°C, 30 minutes at 63°C, and 1 minute at 72°C. Amplified DNA was purified on a Qiagen MinElute column and eluted in 22 μL of Qiagen elution buffer. Purified libraries were assessed using a Bioanalyzer High-Sensitivity DNA Analysis Kit (Agilent). Paired-end 50 bp reads were sequenced at the Center for Epigenetics Research at MSKCC. ATAC-seq reads were 3′ trimmed and filtered for quality and adapter content using version 0.4.5 of TrimGalore, with a quality setting of 15, and running version 1.15 of cutadapt and version 0.11.5 of FastQC. Reads were aligned to mouse assembly mm9 with version 2.3.4.1 of bowtie2 (ref. 85; http://bowtie-bio.sourceforge.net/bowtie2/index.shtml) and were deduplicated using MarkDuplicates in version 2.16.0 of Picard Tools. To ascertain enriched regions, MACS2 (ref. 86; https://github.com/taoliu/MACS) was used with a *P* value setting of 0.001 with input sequence as background control. The BEDTools (87) suite (http://bedtools.readthedocs.io) was used to create normalized read density profiles. A global peak atlas was created by first removing blacklisted regions (http://mitra.stanford.edu/kundaje/akundaje/release/blacklists/mm9-mouse/mm9-blacklist.bed.gz), then merging all peaks within 500 bp and counting reads with version 1.6.1 of featureCounts (ref. 88; http://subread.sourceforge.net). Comparison of intra versus intergroup clustering in principal component analysis was used to determine normalization strategy, using either the median ratio method of DESeq2 or a sequencing depth-based factor normalized to ten million uniquely mapped fragments. Differential enrichment was scored using DESeq2 for all pairwise group contrasts. All differential peaks were then merged for all contrasts in a given data set, and k-means clustering was performed from k = 4 to the point at which cluster groups became redundant. Peak-gene associations were created using linear genomic distance to transcription start site. Motif signatures were obtained using Homer (40) v4.5 (http://homer.ucsd.edu). Composite and tornado plots were created using deepTools (89) v3.3.0 by running computeMatrix and plotHeatmap on normalized bigwigs with average signal sampled in 25 bp windows and flanking region defined by the surrounding 3 kb.

ChIP-seq

ChIP-seq was performed as described previously (90). Briefly, 5 million cells were cross-linked for 10 minutes with 1% PFA, washed, and lysed. Chromatin was sheared using Bioruptor (Diagenode) and incubated with protein A/G magnetic beads (Pierce; cat. #26162) that were preincubated with specific anti-histone antibodies (~7.5 μg of antibody conjugated to 75 μL of beads were used for each ChIP reaction), washed, and eluted. The eluted chromatin was reverse-cross-linked, and DNA was column-purified using MinElute PCR Purification Kit (Qiagen; catalog no. 28004). The following antibodies were used for immunoprecipitation: H3K27ac (Abcam; catalog no. ab4729), H3K4me1 (Abcam; catalog no. ab8895), and H3K4me3 (Cell Signaling Technology catalog no. 9751S).

ChIP-seq libraries were prepared at the Center for Epigenetic Research (MSKCC) using the NEBNext ChIP-seq Library Prep Master Mix Set for Illumina (New England BioLabs) following the manufacturer's instructions. Samples were QC'd using a Bioanalyzer TapeStation (Agilent Technologies 2200) to determine fragment size. Samples were pooled and submitted for SE50 sequencing using an Illumina HiSeq 2500 System at New York Genome Center. Reads were trimmed for quality and Illumina adapter sequences using "trim_galore" before aligning to mouse assembly mm9 with bowtie2 using the default parameters. Aligned reads with the same start site and orientation were removed using the Picard tool MarkDuplicates (http://broadinstitute.github.io/picard/). Density profiles were created by extending each read to the average library fragment size and then computing density using the BEDTools suite (http://bedtools.readthedocs.io). Enriched regions were discovered using MACS2 and scored against matched input libraries (fold change > 2 and $P < 0.001$). Peaks were then filtered against genomic "blacklisted" regions (http://mitra.stanford.edu/kundaje/akundaje/release/blacklists/mm9-mouse/mm9-blacklist.bed.gz)

and those within 500 bp were merged. All genome browser tracks and read density tables were normalized to a sequencing depth of ten million mapped reads. Composite ChIP signal was calculated over each ATAC cluster using normalized bigwig files processed with deepTools v3.3.0.

Derivation of Mouse Thyroid Cancer Cell Lines

To generate mouse tumor cell lines, tumors were dissected, minced in PBS, and resuspended in 10 mL of digestion medium (minimum essential media containing 112 U/mL type I collagenase; Worthington, cat. #CLS-1), 1.2 U/mL dispase (Gibco; catalog no. 17105-041), penicillin (50 U/mL), and streptomycin (50 mg/mL). Cells were incubated at 37°C for 60 minutes with vigorous shaking, after which cells were spun down and resuspended in Coon's modified F12 medium with penicillin/streptomycin/L-glutamine (P/S/G; Gemini; #400-110) and 0.5% bovine brain extract, plated into CellBind plates (Corning Inc.) for two weeks and then switched to Coon's modified F12 medium with P/S/G containing 5% FBS for routine culturing and maintenance. Cell lines were maintained at 37°C and 5% CO_2 in humidified atmosphere and were passaged at least five times prior to use in experiments.

Western Blotting

Cells were harvested with 0.05% tryspin/0.02% EDTA solution, and cell pellets were washed with cold PBS. Proteins were extracted using NE-PER Nuclear and Cytoplasmic Extraction Reagents (Thermo Scientific; catalog no. 78835) as per the manufacturer's instructions. Protein concentrations were estimated by the BCA Kit (Thermo Scientific) on a microplate reader (SpectraMax M5). Comparable amounts of proteins in the nuclear extract were subjected to SDS-PAGE using NuPAGE 4% to 12% Bis–Tris gradient gels (Invitrogen) and were transferred to PVDF membranes. Following overnight incubation with primary antibody at 4°C, membranes were incubated with goat anti-rabbit or goat anti-mouse secondary antibodies coupled to IRDye fluorophores for 1 hour at room temperature, and fluorescence was detected using the Odyssey CLx Imaging System (LI-COR Biosciences). The following primary antibodies were used at 1:1,000 dilution: ARID1A (Bethyl Labs # A301-040A), ARID1B (Abcam # ab57461), ARID2 (Bethyl Labs # A302-230A), SMARCB1 (BD Biosciences; # 612111), SMARCC1 (Santa Cruz Biotechnology; # sc-32763), and β-Actin (Sigma # A2228).

BRD9 Inhibitor Sensitivity Assay

Cells were plated in triplicate into 96-well plates at 5,000 cells per well, and treated with DMSO or increasing concentrations of I-BRD9 (Selleckchem S7835) for 7 days, at which time cell viability was determined using CellTiter-Glo (Promega; #G7572) on a GloMax 96 Microplate Luminometer (Promega) as per the manufacturer's instructions. IC_{50} values were calculated by nonlinear regression using Prism v8.3 (GraphPad Software).

Quantitative Real-Time PCR

Total RNA was isolated using the RNeasy Mini Kit (Qiagen; catalog no. 74104) with on-column DNase digestion according to the manufacturer's instructions. Total RNA (1 μg) was reverse-transcribed into cDNA using SuperScript III Reverse Transcriptase (Invitrogen) using random hexamers. qRT-PCR was carried out in triplicate using Power SYBR Green PCR Master Mix (Applied Biosystems) on the ViiA 7 Real-Time PCR System (Applied Biosystems). Gene-specific primer sets used are shown in Supplementary Table S3. β-actin served as the endogenous normalization control.

Human Clinical Trials

The redifferentiation trials NCT02456701 and NCT02152995 were performed after approval by the MSKCC Institutional Review Board (IRB numbers 15-046 and 13-157, respectively). Written informed consent was obtained from all patients in these studies. We show representative examples of patients enrolled in two redifferentiation clinical trials for RAI-refractory metastatic thyroid cancer: (i) vemurafenib + CDX-3379 (NCT02456701) for $BRAF^{V600E}$-mutant tumors and (ii) trametinib for *RAS*-mutant tumors (NCT02152995). Supplementary Fig. S13A and S13B illustrates the schema for these studies. Briefly, baseline RAI avidity was assessed with ^{124}I PET/CT lesional dosimetry while patients were on a low-iodine diet. Patients were given 0.9 mg thyrotropin alfa (Thyrogen, Sanofi Genzyme) by intramuscular injection on two consecutive days, followed by 6 mCi of ^{124}I by mouth (range, 4.8–7.2 mCi) on the third day. ^{124}I-PET/CT images were obtained on day 5. In the NCT02456701 study, patients received vemurafenib 960 mg orally twice daily for 4 weeks, with the addition of CDX-3379 1,000 mg intravenously every 2 weeks beginning on week 3. For NCT02152995, they were treated with trametinib 2 mg daily for 4 weeks. The ^{124}I PET/CT lesional dosimetry was repeated during the fourth week of therapy. Patients had sequential biopsies of the same index lesion at baseline (prior to drug), at 2 weeks while on vemurafenib, and at 4 weeks while on vemurafenib + CDX-3379 (Trial 1). If at least one index tumor (>5 mm in maximal diameter) was predicted to absorb >2,000 cGy with a clinically administered ^{131}I activity of <300 mCi, the patient was categorized as an ^{124}I responder. Tumor and normal DNA from these patients were profiled by MSK-IMPACT.

RNA-seq of Tissue Biopsies

Serial lesional biopsies were obtained and the samples were flash-frozen. Frozen tissue was homogenized in TRIzol using the Qiagen TissueLyser at 15 Hz for 2–3 minutes with a Stainless Steel Bead (Qiagen cat. #69989). Phase separation was induced with chloroform. RNA was precipitated with isopropanol and linear acrylamide and washed with 75% ethanol. The samples were resuspended in RNase-free water. After RiboGreen quantification and quality control by Agilent BioAnalyzer, 66 ng–1 μg of total RNA underwent ribosomal depletion and library preparation using the TruSeq Stranded Total RNA LT Kit (Illumina; catalog no. RS-122-1202) with 6 cycles of PCR. Samples were barcoded and run on a HiSeq 2500 in High Output mode or HiSeq 4000 in a 50 bp/50 bp paired-end run, using the TruSeq SBS Kit v4 or HiSeq 3000/4000 SBS Kit (Illumina). On average, 96 million paired reads were generated per sample and 30% of the data were mapped to the transcriptome. Reads were aligned to human reference genome hg19 using STAR aligner 2.5.3a and normalized using Fragments Per Kilobase of transcripts per million mapped reads (FPKM) using Partek Flow software (Partek Inc.). The MAPK output score was computed using the 52 genes described by Pratilas and colleagues (54). The MAPK output score and enhanced thyroid differentiation scores (eTDS) were calculated from RNA-seq data as described previously (9, 53).

Statistical Analysis

The statistical software GraphPad-Prism (version 8.0; GraphPad Software, Inc.) was used to analyze the data. All data for qRT-PCR/RNA-seq expression values, ultrasonography, immunofluorescence image quantification, and autoradiography are represented as mean ± SEM, and *P* values were calculated using unpaired two-tailed Student *t* tests. For Kaplan–Meier survival analyses, *P* values were calculated using log-rank Mantel–Cox test. For comparison of mouse tumor H&E sections for tumor progression Fisher exact test was used to calculate the *P* value. A *P* value of <0.05 was considered statistically significant.

The correlation of RNA-seq with ATAC clusters in response to vehicle versus CKI in Fig. 4D and E was evaluated in the following way: for each ATAC cluster, the number of gene associations with that cluster was used to create a size-matched sampling from the gene-expression matrix, keeping group (genotype) assignments, but shuffling the rows (genes), then collapsing to z-score, and testing

how often the cluster with the ATAC-enriched signal has an expression *z*-score at least as high as that observed in the actual linked RNA-seq data. One million shuffles were performed per cluster.

Accession Codes

ATAC-seq, RNA-seq, and ChIP-seq data from this study have been submitted to the NCBI Gene-Expression Omnibus under GEO Superseries ID GSE147479.

Authors' Disclosures

M. Saqcena reports grants from NIH/NCI and Memorial Sloan Kettering Cancer Center during the conduct of the study. R. Ghossein reports grants from NIH P30CA008748 during the conduct of the study. P. Chi reports grants and personal fees from Deciphera, personal fees from Exelixis and Zai Lab, grants from Array/Pfizer, NIH/NCI, FDA/OPD, and NTAP/Bloomberg Foundation outside the submitted work. A.L. Ho reports grants from Celldex and NIH during the conduct of the study; grants, personal fees, and non-financial support from Ayala, grants and non-financial support from Merck, non-financial support from Klus Pharma, personal fees from Curevac, Shanghai Jia Tong University, McGivney Advisors, Mass General Hospital, Prelude Therapeutics, NCI, Rgenta, Winship/Emory, and Regeneron, grants and personal fees from Kura Oncology, Eisai, grants from BMS, Novartis, AstraZeneca, Celldex, Genentech Roche, Bayer, Elevar Therapeutics, and Astellas outside the submitted work. J.A. Fagin reports grants from NIH RO1-CA50706-23, NIH-P50-CA 172012-05, NIH-P30-CA08748, NIH-CA-184724, and Cycle for Survival during the conduct of the study; grants from Eisai and personal fees from Loxo Oncology outside the submitted work. No other disclosures were reported.

Authors' Contributions

M. Saqcena: Conceptualization, resources, data curation, software, formal analysis, supervision, funding acquisition, validation, investigation, visualization, methodology, writing–original draft, project administration, writing–review and editing. **E. de Stanchina:** Data curation and methodology. **B. Xu:** Resources, methodology, writing–review and editing. **X.H. Liao:** Data curation and methodology. **S. Refetoff:** Conceptualization, formal analysis, and methodology. **R. Ghossein:** Resources, data curation, formal analysis, investigation, methodology, writing–review and editing. **P. Chi:** Conceptualization, formal analysis, writing–review and editing. **A.L. Ho:** Conceptualization, resources, formal analysis, funding acquisition, investigation, writing–review and editing. **R.P. Koche:** Conceptualization, data curation, software, formal analysis, investigation, visualization, methodology, writing–review and editing. **J.A. Fagin:** Conceptualization, resources, formal analysis, supervision, funding acquisition, investigation, visualization, writing–original draft, project administration, writing–review and editing. **L.J. Leandro-Garcia:** Conceptualization, resources, data curation, software, formal analysis, supervision, funding acquisition, validation, investigation, visualization, methodology, writing–original draft, project administration, writing–review and editing. **J.L.V. Maag:** Data curation, software, formal analysis, visualization, and methodology. **V. Tchekmedyian:** Data curation, formal analysis, and investigation. **G.P. Krishnamoorthy:** Conceptualization, data curation, formal analysis, investigation, and methodology. **P.P. Tamarapu:** Data curation and methodology. **V. Tiedje:** Data curation and methodology. **V. Reuter:** Data curation, software, formal analysis, visualization, and methodology. **J.A. Knauf:** Conceptualization, investigation, writing–review and editing.

Acknowledgments

We thank Dr. Charles W.M. Roberts (St. Jude Children's Research Hospital) for providing us with *Smarcb1*$^{fl/fl}$ mice, Dr. Zhong Wang (University of Michigan) for the *Arid1a*$^{fl/fl}$ mice, Dr. Shioko Kimura (NCI) for the *TPO-Cre* mice, and Dr. Catrin Pritchard (University of Leicester, UK) for the *LSL-Braf*$^{V600E/+}$ mice. We also thank Drs. Cigall Kadoch (Dana-Farber Cancer Institute and Harvard Medical School) and Charles W.M. Roberts for helpful discussions. This work was supported by grants from the NIH CA50706-23 (J.A. Fagin), CA184724-01A1 (A.L. Ho and J.A. Fagin), and DK-15070 (S. Refetoff), Cycle for Survival (A.L. Ho), Geoffrey Beene Cancer Research Center (J.A. Fagin and A.L. Ho), NCI Thyroid Cancer SPORE P50 CA 172012-01 (J.A. Fagin and M. Saqcena), and the Translational Research Oncology Training program 5T32CA160001 (M. Saqcena). The vemurafenib plus CDX-3379 clinical trial was funded by Celldex Therapeutics (formerly Koltan Pharmaceuticals prior to its acquisition by Celldex). We thank the MSKCC Research Animal Resource Center and the following core facilities for their support: Molecular Cytology, Flow Cytometry, Pathology, and the Integrative Genomics Operation funded by the NCI Cancer Center Support Grant (CCSG; P30 CA08748), Cycle for Survival, and the Marie-Josée and Henry R. Kravis Center for Molecular Oncology.

The costs of publication of this article were defrayed in part by the payment of page charges. This article must therefore be hereby marked *advertisement* in accordance with 18 U.S.C. Section 1734 solely to indicate this fact.

Received May 22, 2020; revised October 16, 2020; accepted December 9, 2020; published first December 14, 2020.

REFERENCES

1. Grignani F, Ferrucci PF, Testa U, Talamo G, Fagioli M, Alcalay M, et al. The acute promyelocytic leukemia-specific PML-RAR alpha fusion protein inhibits differentiation and promotes survival of myeloid precursor cells. Cell 1993;74:423–31.
2. Stahl M, Tallman MS. Acute promyelocytic leukemia (APL): remaining challenges towards a cure for all. Leuk Lymphoma 2019;60:3107–15.
3. Ward PS, Patel J, Wise DR, Abdel-Wahab O, Bennett BD, Coller HA, et al. The common feature of leukemia-associated IDH1 and IDH2 mutations is a neomorphic enzyme activity converting alpha-ketoglutarate to 2-hydroxyglutarate. Cancer Cell 2010;17:225–34.
4. Figueroa ME, Abdel-Wahab O, Lu C, Ward PS, Patel J, Shih A, et al. Leukemic IDH1 and IDH2 mutations result in a hypermethylation phenotype, disrupt TET2 function, and impair hematopoietic differentiation. Cancer Cell 2010;18:553–67.
5. DiNardo CD, Stein EM, de Botton S, Roboz GJ, Altman JK, Mims AS, et al. Durable remissions with ivosidenib in IDH1-mutated relapsed or refractory AML. N Engl J Med 2018;378:2386–98.
6. Kimura ET, Nikiforova MN, Zhu Z, Knauf JA, Nikiforov YE, Fagin JA. High prevalence of BRAF mutations in thyroid cancer: genetic evidence for constitutive activation of the RET/PTC-RAS-BRAF signaling pathway in papillary thyroid carcinoma. Cancer Res 2003;63:1454–7.
7. Cohen Y, Xing M, Mambo E, Guo Z, Wu G, Trink B, et al. BRAF mutation in papillary thyroid carcinoma. J Natl Cancer Inst 2003;95:625–7.
8. Frattini M, Ferrario C, Bressan P, Balestra D, De Cecco L, Mondellini P, et al. Alternative mutations of BRAF, RET and NTRK1 are associated with similar but distinct gene expression patterns in papillary thyroid cancer. Oncogene 2004;23:7436–40.
9. Cancer Genome Atlas Research Network. Integrated genomic characterization of papillary thyroid carcinoma. Cell 2014;159:676–90.
10. Landa I, Ibrahimpasic T, Boucai L, Sinha R, Knauf JA, Shah RH, et al. Genomic and transcriptomic hallmarks of poorly differentiated and anaplastic thyroid cancers. J Clin Invest 2016;126:1052–66.
11. Kunstman JW, Juhlin CC, Goh G, Brown TC, Stenman A, Healy JM, et al. Characterization of the mutational landscape of anaplastic thyroid cancer via whole-exome sequencing. Hum Mol Genet 2015;24:2318–29.
12. Shi X, Liu R, Qu S, Zhu G, Bishop J, Liu X, et al. Association of TERT promoter mutation 1,295,228 C>T with BRAF V600E mutation,

older patient age, and distant metastasis in anaplastic thyroid cancer. J Clin Endocrinol Metab 2015;100:E632–7.
13. Landa I, Ganly I, Chan TA, Mitsutake N, Matsuse M, Ibrahimpasic T, et al. Frequent somatic TERT promoter mutations in thyroid cancer: higher prevalence in advanced forms of the disease. J Clin Endocrinol Metab 2013;98:E1562–6.
14. Donghi R, Longoni A, Pilotti S, Michieli P, Della Porta G, Pierotti MA. Gene p53 mutations are restricted to poorly differentiated and undifferentiated carcinomas of the thyroid gland. J Clin Invest 1993;91:1753–60.
15. Fagin JA, Matsuo K, Karmakar A, Chen DL, Tang SH, Koeffler HP. High prevalence of mutations of the p53 gene in poorly differentiated human thyroid carcinomas. J Clin Invest 1993;91:179–84.
16. Montero-Conde C, Leandro-Garcia LJ, Chen X, Oler G, Ruiz-Llorente S, Ryder M, et al. Transposon mutagenesis identifies chromatin modifiers cooperating with Ras in thyroid tumorigenesis and detects ATXN7 as a cancer gene. Proc Natl Acad Sci U S A 2017;114:E4951–E60.
17. Alver BH, Kim KH, Lu P, Wang X, Manchester HE, Wang W, et al. The SWI/SNF chromatin remodelling complex is required for maintenance of lineage specific enhancers. Nat Commun 2017;8:14648.
18. Mashtalir N, D'Avino AR, Michel BC, Luo J, Pan J, Otto JE, et al. Modular organization and assembly of SWI/SNF family chromatin remodeling complexes. Cell 2018;175:1272–88.
19. Gatchalian J, Malik S, Ho J, Lee DS, Kelso TWR, Shokhirev MN, et al. A non-canonical BRD9-containing BAF chromatin remodeling complex regulates naive pluripotency in mouse embryonic stem cells. Nat Commun 2018;9:5139.
20. Kadoch C, Hargreaves DC, Hodges C, Elias L, Ho L, Ranish J, et al. Proteomic and bioinformatic analysis of mammalian SWI/SNF complexes identifies extensive roles in human malignancy. Nat Genet 2013;45:592–601.
21. Wang X, Haswell JR, Roberts CW. Molecular pathways: SWI/SNF (BAF) complexes are frequently mutated in cancer–mechanisms and potential therapeutic insights. Clin Cancer Res 2014;20:21–7.
22. Ho L, Jothi R, Ronan JL, Cui K, Zhao K, Crabtree GR. An embryonic stem cell chromatin remodeling complex, esBAF, is an essential component of the core pluripotency transcriptional network. Proc Natl Acad Sci U S A 2009;106:5187–91.
23. Wilson BG, Wang X, Shen X, McKenna ES, Lemieux ME, Cho YJ, et al. Epigenetic antagonism between polycomb and SWI/SNF complexes during oncogenic transformation. Cancer Cell 2010;18:316–28.
24. Knutson SK, Warholic NM, Wigle TJ, Klaus CR, Allain CJ, Raimondi A, et al. Durable tumor regression in genetically altered malignant rhabdoid tumors by inhibition of methyltransferase EZH2. Proc Natl Acad Sci U S A 2013;110:7922–7.
25. Bitler BG, Aird KM, Garipov A, Li H, Amatangelo M, Kossenkov AV, et al. Synthetic lethality by targeting EZH2 methyltransferase activity in ARID1A-mutated cancers. Nat Med 2015;21:231–8.
26. Wu JN, Roberts CW. ARID1A mutations in cancer: another epigenetic tumor suppressor? Cancer Discov 2013;3:35–43.
27. Fernandez LP, Lopez-Marquez A, Santisteban P. Thyroid transcription factors in development, differentiation and disease. Nat Rev Endocrinol 2015;11:29–42.
28. Antonica F, Kasprzyk DF, Opitz R, Iacovino M, Liao XH, Dumitrescu AM, et al. Generation of functional thyroid from embryonic stem cells. Nature 2012;491:66–71.
29. Chakravarty D, Santos E, Ryder M, Knauf JA, Liao XH, West BL, et al. Small-molecule MAPK inhibitors restore radioiodine incorporation in mouse thyroid cancers with conditional BRAF activation. J Clin Invest 2011;121:4700–11.
30. Nagarajah J, Le M, Knauf JA, Ferrandino G, Montero-Conde C, Pillarsetty N, et al. Sustained ERK inhibition maximizes responses of BrafV600E thyroid cancers to radioiodine. J Clin Invest 2016;126:4119–24.
31. Ho AL, Grewal RK, Leboeuf R, Sherman EJ, Pfister DG, Deandreis D, et al. Selumetinib-enhanced radioiodine uptake in advanced thyroid cancer. N Engl J Med 2013;368:623–32.
32. Rothenberg SM, McFadden DG, Palmer EL, Daniels GH, Wirth LJ. Redifferentiation of iodine-refractory BRAF V600E-mutant metastatic papillary thyroid cancer with dabrafenib. Clin Cancer Res 2015;21:1028–35.
33. Helming KC, Wang X, Wilson BG, Vazquez F, Haswell JR, Manchester HE, et al. ARID1B is a specific vulnerability in ARID1A-mutant cancers. Nat Med 2014;20:251–4.
34. Hargreaves DC, Crabtree GR. ATP-dependent chromatin remodeling: genetics, genomics and mechanisms. Cell Res 2011;21:396–420.
35. Sun X, Chuang JC, Kanchwala M, Wu L, Celen C, Li L, et al. Suppression of the SWI/SNF component Arid1a promotes mammalian regeneration. Cell Stem Cell 2016;18:456–66.
36. Trueba SS, Auge J, Mattei G, Etchevers H, Martinovic J, Czernichow P, et al. PAX8, TITF1, and FOXE1 gene expression patterns during human development: new insights into human thyroid development and thyroid dysgenesis-associated malformations. J Clin Endocrinol Metab 2005;90:455–62.
37. Mathur R, Alver BH, San Roman AK, Wilson BG, Wang X, Agoston AT, et al. ARID1A loss impairs enhancer-mediated gene regulation and drives colon cancer in mice. Nat Genet 2017;49:296–302.
38. Wang X, Lee RS, Alver BH, Haswell JR, Wang S, Mieczkowski J, et al. SMARCB1-mediated SWI/SNF complex function is essential for enhancer regulation. Nat Genet 2017;49:289–95.
39. Nakayama RT, Pulice JL, Valencia AM, McBride MJ, McKenzie ZM, Gillespie MA, et al. SMARCB1 is required for widespread BAF complex-mediated activation of enhancers and bivalent promoters. Nat Genet 2017;49:1613–23.
40. Heinz S, Benner C, Spann N, Bertolino E, Lin YC, Laslo P, et al. Simple combinations of lineage-determining transcription factors prime cis-regulatory elements required for macrophage and B cell identities. Mol Cell 2010;38:576–89.
41. Michel BC, D'Avino AR, Cassel SH, Mashtalir N, McKenzie ZM, McBride MJ, et al. A non-canonical SWI/SNF complex is a synthetic lethal target in cancers driven by BAF complex perturbation. Nat Cell Biol 2018;20:1410–20.
42. Wang X, Wang S, Troisi EC, Howard TP, Haswell JR, Wolf BK, et al. BRD9 defines a SWI/SNF sub-complex and constitutes a specific vulnerability in malignant rhabdoid tumors. Nat Commun 2019;10:1881.
43. Fernandez LP, Lopez-Marquez A, Martinez AM, Gomez-Lopez G, Santisteban P. New insights into FoxE1 functions: identification of direct FoxE1 targets in thyroid cells. PLoS One 2013;8:e62849.
44. Civitareale D, Lonigro R, Sinclair AJ, Di Lauro R. A thyroid-specific nuclear protein essential for tissue-specific expression of the thyroglobulin promoter. EMBO J 1989;8:2537–42.
45. Francis-Lang H, Price M, Polycarpou-Schwarz M, Di Lauro R. Cell-type-specific expression of the rat thyroperoxidase promoter indicates common mechanisms for thyroid-specific gene expression. Mol Cell Biol 1992;12:576–88.
46. Zannini M, Francis-Lang H, Plachov D, Di Lauro R. Pax-8, a paired domain-containing protein, binds to a sequence overlapping the recognition site of a homeodomain and activates transcription from two thyroid-specific promoters. Mol Cell Biol 1992;12:4230–41.
47. Taki K, Kogai T, Kanamoto Y, Hershman JM, Brent GA. A thyroid-specific far-upstream enhancer in the human sodium/iodide symporter gene requires Pax-8 binding and cyclic adenosine 3′,5′-monophosphate response element-like sequence binding proteins for full activity and is differentially regulated in normal and thyroid cancer cells. Mol Endocrinol 2002;16:2266–82.
48. Franco AT, Malaguarnera R, Refetoff S, Liao XH, Lundsmith E, Kimura S, et al. Thyrotrophin receptor signaling dependence of Braf-induced thyroid tumor initiation in mice. Proc Natl Acad Sci U S A 2011;108:1615–20.
49. Ishii N, Harada N, Joseph EW, Ohara K, Miura T, Sakamoto H, et al. Enhanced inhibition of ERK signaling by a novel allosteric MEK inhibitor, CH5126766, that suppresses feedback reactivation of RAF activity. Cancer Res 2013;73:4050–60.
50. Theodoulou NH, Bamborough P, Bannister AJ, Becher I, Bit RA, Che KH, et al. Discovery of I-BRD9, a selective cell active chemical probe for bromodomain containing protein 9 inhibition. J Med Chem 2016;59:1425–39.
51. Brien GL, Remillard D, Shi J, Hemming ML, Chabon J, Wynne K, et al. Targeted degradation of BRD9 reverses oncogenic gene expression in synovial sarcoma. Elife 2018;7:e41305.

52. Montero-Conde C, Ruiz-Llorente S, Dominguez JM, Knauf JA, Viale A, Sherman EJ, et al. Relief of feedback inhibition of HER3 transcription by RAF and MEK inhibitors attenuates their antitumor effects in BRAF-mutant thyroid carcinomas. Cancer Discov 2013;3:520–33.
53. Dunn LA, Sherman EJ, Baxi SS, Tchekmedyian V, Grewal RK, Larson SM, et al. Vemurafenib redifferentiation of BRAF mutant, RAI-refractory thyroid cancers. J Clin Endocrinol Metab 2019;104:1417–28.
54. Pratilas CA, Taylor BS, Ye Q, Viale A, Sander C, Solit DB, et al. (V600E)BRAF is associated with disabled feedback inhibition of RAF-MEK signaling and elevated transcriptional output of the pathway. Proc Natl Acad Sci U S A 2009;106:4519–24.
55. Durante C, Puxeddu E, Ferretti E, Morisi R, Moretti S, Bruno R, et al. BRAF mutations in papillary thyroid carcinomas inhibit genes involved in iodine metabolism. J Clin Endocrinol Metab 2007;92:2840–3.
56. Xing M, Westra WH, Tufano RP, Cohen Y, Rosenbaum E, Rhoden KJ, et al. BRAF mutation predicts a poorer clinical prognosis for papillary thyroid cancer. J Clin Endocrinol Metab 2005;90:6373–9.
57. Lito P, Pratilas CA, Joseph EW, Tadi M, Halilovic E, Zubrowski M, et al. Relief of profound feedback inhibition of mitogenic signaling by RAF inhibitors attenuates their activity in BRAFV600E melanomas. Cancer Cell 2012;22:668–82.
58. The Cancer Genome Atlas Research Network. Integrated genomic characterization of papillary thyroid carcinoma. Cell 2014;159:676–90.
59. Wang J, Knauf JA, Basu S, Puxeddu E, Kuroda H, Santoro M, et al. Conditional expression of RET/PTC induces a weak oncogenic drive in thyroid PCCL3 cells and inhibits thyrotropin action at multiple levels. Mol Endocrinol 2003;17:1425–36.
60. Baratta MG, Porreca I, Di Lauro R. Oncogenic ras blocks the cAMP pathway and dedifferentiates thyroid cells via an impairment of pax8 transcriptional activity. Mol Endocrinol 2009;23:838–48.
61. Mitsutake N, Knauf JA, Mitsutake S, Mesa C Jr, Zhang L, Fagin JA. Conditional BRAFV600E expression induces DNA synthesis, apoptosis, dedifferentiation, and chromosomal instability in thyroid PCCL3 cells. Cancer Res 2005;65:2465–73.
62. Missero C, Pirro MT, Di Lauro R. Multiple ras downstream pathways mediate functional repression of the homeobox gene product TTF-1. Mol Cell Biol 2000;20:2783–93.
63. Riesco-Eizaguirre G, Rodriguez I, De l V, Costamagna E, Carrasco N, Nistal M, et al. The BRAFV600E oncogene induces transforming growth factor beta secretion leading to sodium iodide symporter repression and increased malignancy in thyroid cancer. Cancer Res 2009;69:8317–25.
64. Cuesta I, Zaret KS, Santisteban P. The forkhead factor FoxE1 binds to the thyroperoxidase promoter during thyroid cell differentiation and modifies compacted chromatin structure. Mol Cell Biol 2007;27:7302–14.
65. Kusakabe T, Kawaguchi A, Kawaguchi R, Feigenbaum L, Kimura S. Thyrocyte-specific expression of Cre recombinase in transgenic mice. Genesis 2004;39:212–6.
66. Saad AG, Kumar S, Ron E, Lubin JH, Stanek J, Bove KE, et al. Proliferative activity of human thyroid cells in various age groups and its correlation with the risk of thyroid cancer after radiation exposure. J Clin Endocrinol Metab 2006;91:2672–7.
67. Castro MR, Bergert ER, Goellner JR, Hay ID, Morris JC. Immunohistochemical analysis of sodium iodide symporter expression in metastatic differentiated thyroid cancer: correlation with radioiodine uptake. J Clin Endocrinol Metab 2001;86:5627–32.
68. Kim KH, Kim W, Howard TP, Vazquez F, Tsherniak A, Wu JN, et al. SWI/SNF-mutant cancers depend on catalytic and non-catalytic activity of EZH2. Nat Med 2015;21:1491–6.
69. Yates LR, Knappskog S, Wedge D, Farmery JHR, Gonzalez S, Martincorena I, et al. Genomic evolution of breast cancer metastasis and relapse. Cancer Cell 2017;32:169–84.
70. Sun XX, Wang SC, Wei YL, Luo X, Jia YM, Li L, et al. Arid1a has context-dependent oncogenic and tumor suppressor functions in liver cancer. Cancer Cell 2017;32:574–89.
71. Nagarajan S, Rao SV, Sutton J, Cheeseman D, Dunn S, Papachristou EK, et al. ARID1A influences HDAC1/BRD4 activity, intrinsic proliferative capacity and breast cancer treatment response. Nat Genet 2020;52:187–97.
72. Xu G, Chhangawala S, Cocco E, Razavi P, Cai Y, Otto JE, et al. ARID1A determines luminal identity and therapeutic response in estrogen-receptor-positive breast cancer. Nat Genet 2020;52:198–207.
73. Rubino C, De VF, Dottorini ME, Hall P, Schvartz C, Couette JE, et al. Second primary malignancies in thyroid cancer patients. Br J Cancer 2003;89:1638–44.
74. Mendoza A, Shaffer B, Karakla D, Mason ME, Elkins D, Goffman TE. Quality of life with well-differentiated thyroid cancer: treatment toxicities and their reduction. Thyroid 2004;14:133–40.
75. Molenaar RJ, Sidana S, Radivoyevitch T, Advani AS, Gerds AT, Carraway HE, et al. Risk of hematologic malignancies after radioiodine treatment of well-differentiated thyroid cancer. J Clin Oncol 2018;36:1831–9.
76. Gao J, Aksoy BA, Dogrusoz U, Dresdner G, Gross B, Sumer SO, et al. Integrative analysis of complex cancer genomics and clinical profiles using the cBioPortal. Sci Signal 2013;6:pl1.
77. Gao X, Tate P, Hu P, Tjian R, Skarnes WC, Wang Z. ES cell pluripotency and germ-layer formation require the SWI/SNF chromatin remodeling component BAF250a. Proc Natl Acad Sci U S A 2008;105:6656–61.
78. Roberts CW, Leroux MM, Fleming MD, Orkin SH. Highly penetrant, rapid tumorigenesis through conditional inversion of the tumor suppressor gene Snf5. Cancer Cell 2002;2:415–25.
79. Mercer K, Giblett S, Green S, Lloyd D, DaRocha Dias S, Plumb M, et al. Expression of endogenous oncogenic V600EB-raf induces proliferation and developmental defects in mice and transformation of primary fibroblasts. Cancer Res 2005;65:11493–500.
80. Pohlenz J, Maqueem A, Cua K, Weiss RE, Van Sande J, Refetoff S. Improved radioimmunoassay for measurement of mouse thyrotropin in serum: strain differences in thyrotropin concentration and thyrotroph sensitivity to thyroid hormone. Thyroid 1999;9:1265–71.
81. Dobin A, Gingeras TR. Mapping RNA-seq reads with STAR. Curr Protoc Bioinformatics 2015;51:11.14.1–19.
82. Anders S, Pyl PT, Huber W. HTSeq–a Python framework to work with high-throughput sequencing data. Bioinformatics 2015;31:166–9.
83. Love MI, Huber W, Anders S. Moderated estimation of fold change and dispersion for RNA-seq data with DESeq2. Genome Biol 2014;15:550.
84. Buenrostro JD, Giresi PG, Zaba LC, Chang HY, Greenleaf WJ. Transposition of native chromatin for fast and sensitive epigenomic profiling of open chromatin, DNA-binding proteins and nucleosome position. Nat Methods 2013;10:1213–8.
85. Langmead B, Salzberg SL. Fast gapped-read alignment with Bowtie 2. Nat Methods 2012;9:357–9.
86. Zhang Y, Liu T, Meyer CA, Eeckhoute J, Johnson DS, Bernstein BE, et al. Model-based analysis of ChIP-Seq (MACS). Genome Biol 2008;9:R137.
87. Quinlan AR, Hall IM. BEDTools: a flexible suite of utilities for comparing genomic features. Bioinformatics 2010;26:841–2.
88. Liao Y, Smyth GK, Shi W. featureCounts: an efficient general purpose program for assigning sequence reads to genomic features. Bioinformatics 2014;30:923–30.
89. Ramirez F, Dundar F, Diehl S, Gruning BA, Manke T. deepTools: a flexible platform for exploring deep-sequencing data. Nucleic Acids Res 2014;42(Web Server issue):W187–91.
90. Goldberg AD, Banaszynski LA, Noh KM, Lewis PW, Elsaesser SJ, Stadler S, et al. Distinct factors control histone variant H3.3 localization at specific genomic regions. Cell 2010;140:678–91.